J. Fluid Mech. (2005), *vol.* 530, *pp.* 31–80.
doi:10.1017/S0022112005003575 Printed in the United Kingdom

Fluid dynamics of floating particles

By P. SINGH[1] AND D. D. JOSEPH[2]

[1]Department of Mechanical Engineering, New Jersey Institute of Technology, Newark, NJ 07102, USA
singhp@njit.edu

[2]Department of Aerospace Engineering and Mechanics, University of Minnesota, Minneapolis, MN 55455, USA
joseph@aem.umn.edu

(Received 14 March 2003 and in revised form 5 November 2004)

We have developed a numerical package to simulate particle motions in fluid interfaces. The particles are moved in a direct simulation respecting the fundamental equations of motion of fluids and solid particles without the use of models. The fluid–particle motion is resolved by the method of distributed Lagrange multipliers and the interface is moved by the method of level sets. The present work fills a gap since there are no other theoretical methods available to describe the nonlinear fluid dynamics of capillary attraction.

Two different cases of constrained motions of floating particles are studied here. In the first case, we study motions of floating spheres under the constraint that the contact angle is fixed by the Young–Dupré law; the contact line must move when the contact angle is fixed. In the second case, we study motions of disks (short cylinders) with flat ends in which the contact line is pinned at the sharp edge of the disk; the contact angle must change when the disks move and this angle can change within the limits specified by the Gibbs extension to the Young–Dupré law. The fact that sharp edged particles cling to interfaces independent of particle wettability is not fully appreciated and needs study.

The numerical scheme presented here is at present the only one which can move floating particles in direct simulation. We simulate the evolution of single heavier-than-liquid spheres and disks to their equilibrium depth and the evolution to clusters of two and fours spheres and two disks under lateral forces, collectively called capillary attraction. New experiments by Wang, Bai & Joseph on the equilibrium depth of floating disks pinned at the edge are presented and compared with analysis and simulations.

1. Introduction

In the work which follows, we will be considering the motions of particles which float in the interface between two fluids. We shall sometimes describe the wettability properties of the particles as hydrophobic or hydrophilic. The mathematical description of our problem in terms of air and water is only a convention for the general problem of motion of particles in the interfaces between any two fluids.

It is well known that small tea leaves floating on the tea surface collect near the cup wall due to the formation of a meniscus that rises near the wall and results in a net capillary force towards the wall. The meniscus rises near the wall because the water wets the cup. If, on the other hand, the liquid does not wet the cup, i.e. the meniscus falls near the cup wall, small floating particles tend to move away from the wall and

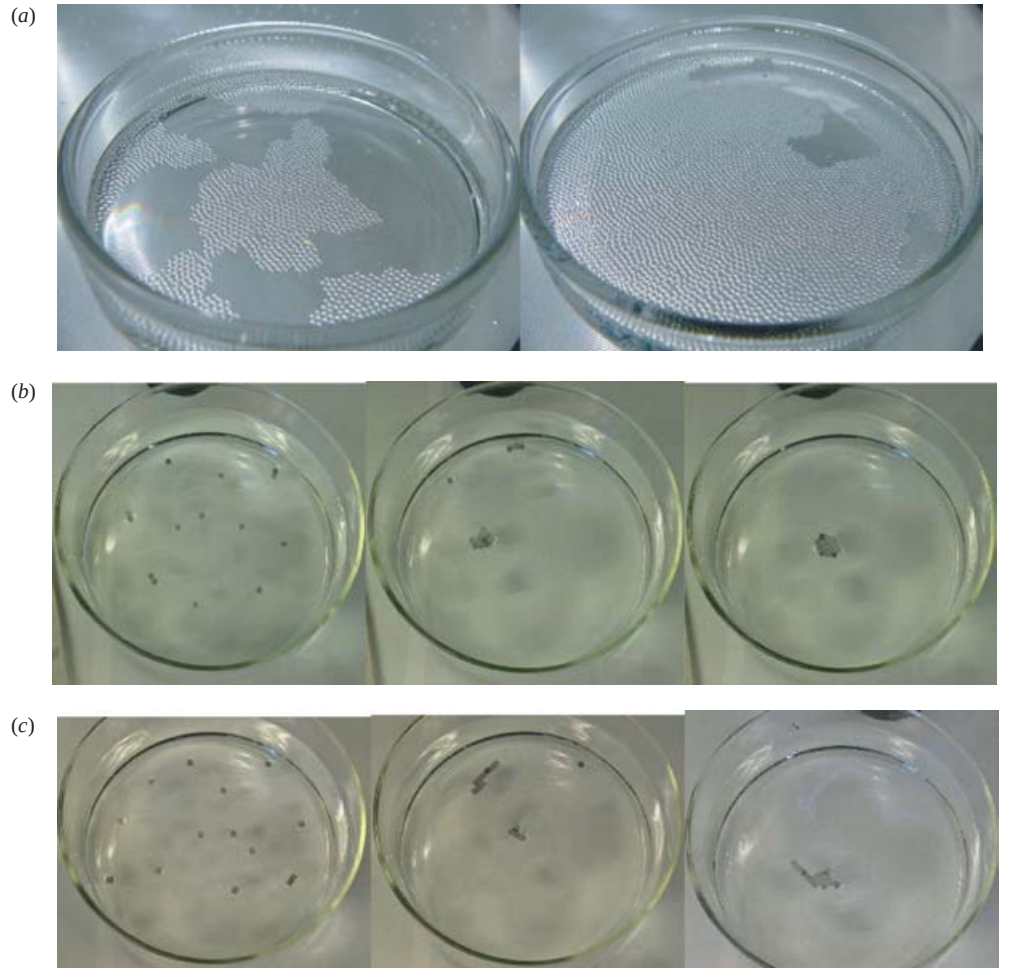

FIGURE 1. (From WBJ 2005) Capillary attraction of floating particles. (*a*) Neutrally buoyant copolymer particles of nominal diameter 0.1 cm cluster in a water/air interface. (*b*) Heavy aluminum disks (short cylinders with circular cross-sections) hanging in a water/air interface at the sharp rim. The distributions of 14 particles at 0 s (left), after 60 s (middle) and after 200 s (right) are shown. The diameter of the disks is 0.3175 cm and their height is 0.15875 cm. (*c*) Heavy aluminum bricks with square cross-sections hanging in a water/air interface at the sharp corners. The distributions of 14 particles at 0 s (left), after 142 s (middle) and after 220 s (right) are shown. The dimension of the bricks is $0.3175\,\text{cm} \times 0.3175\,\text{cm} \times 0.15875\,\text{cm}$. The attractive power of capillarity on floating particles is very long range and the accelerations in the final stage of clustering are exceedingly large. Movies of these experiments can be viewed at http://www.aem.umn.edu/research/particles/floating/.

toward the centre of the cup. Similarly, the deformation of liquid–liquid interfaces due to floating light particles, or due to trapped heavy particles, gives rise to capillary forces on the particles which cause them to cluster, as can be seen in figure 1. The clustering of particles on interfaces is important because it modifies the interfacial properties of the two-phase system and is used in many flotation-based extraction and separation processes (Gerson, Zaijc & Ouchi 1979). More recently, this effect has been used for the self-assembly of submicron sized particles on two-liquid interfaces (see Bowden *et al.* 1997, 1999; Grzybowski *et al.* 2001, and references therein).

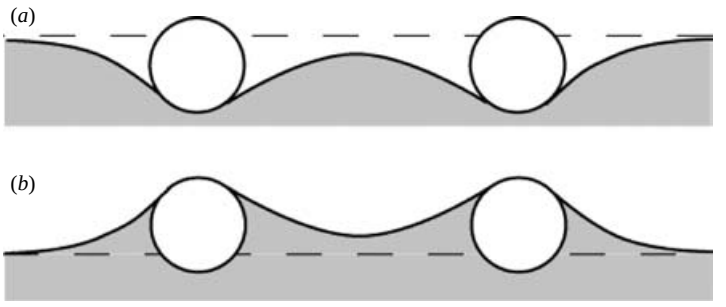

FIGURE 2. Spherical particles in water. (*a*) Heavier-than-water hydrophobic spheres. The meniscus between the spheres is below the undisturbed level. Assuming that the contact angle remains fixed, the horizontal component of capillary force moves them toward each other. (*b*) Lighter-than-water hydrophilic spheres will rise into the elevated section of the meniscus and come together.

The motion of tea leaves towards or away from the wall, in the above example, is entirely due to the deformation of the meniscus near the cup wall. The clustering of particles, on the other hand, is a consequence of the interface deformation caused by neighbouring particles. Specifically, when two heavy hydrophobic spheres are close to each other the deformed interface around the spheres is not symmetric because the interface height between the spheres is lowered by the capillary force; on the other hand, lighter-than-water hydrophilic spheres will rise as shown in figure 2. In both of these cases, the lateral component of interfacial tension is attractive and the spheres tend to cluster. But, when one sphere is hydrophilic and the other is hydrophobic, the lateral force at short range is repulsive and tight clusters cannot form.

The literature on capillary attraction is cited by Kralchevsky & Nagayama (2000) and Saif (2002), here in § 3, and in the paper on capillary attraction of particles embedded in a thin film rimming the inside of a rotating cylinder by Joseph *et al.* (2003). These works do not treat the case of capillary attraction of particles pinned to the interface at a sharp edge which is one of the main subjects in this paper.

Problems of evolution to equilibrium of heavier-than-liquid floating particles may be studied by direct numerical simulation (DNS); this simulation method fills a gap identified by Gifford & Scriven (1971) who noted that

> "casual observations... show that floating needles and many other sorts of particles do indeed come together with astonishing acceleration. The unsteady flow fields that are generated challenge analysis by both experiment and theory. They will have to be understood before the commonplace 'capillary attraction' can be more than a mere label, so far as dynamic processes are concerned."

The basic facts about the equilibrium of single particles are discussed in § 2 and new experiments on the equilibrium depth of disks pinned at their edges are presented. The literature on capillary attraction is briefly reviewed in § 3. In § 4 we set out the equations which govern the motions of floating particles and introduce the basic dimensionless groups which characterize these motions. In § 5, we outline the numerical method stressing only those details which are new. Readers interested in constructing or improving the numerical algorithm used in this study can find a detailed description in the Appendix. In § 6.1, we compute the solutions of the initial value problems, starting from rest, for one, two and four spheres with contact angle prescribed. In § 6.1, we compute the solutions of the initial value problems, starting

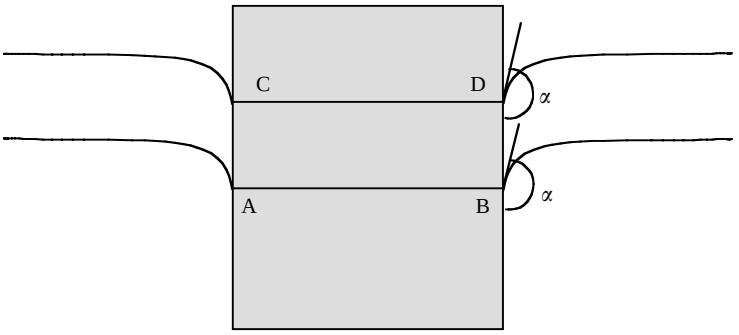

FIGURE 3. The vertical component of capillary force for the disk does not change when the contact line moves from AB to CD, for two different floating heights, because the contact angle α is fixed. For a sphere, the vertical component of the capillary force changes as the contact line moves on its surface.

from rest, for one and two disks pinned at their sharp edges. The solutions are compared with experimental data.

2. Floating particles which should sink

In this section we consider the forces that determine the equilibrium depth of a floating particle. Princen (1969) gave an excellent analysis of this problem for a sphere and prismatic particles with sharp edges. Keller (1998) generalized this analysis for smooth bodies of arbitrary shape. Katoh, Fujita & Imazu (1992) used the floating ball to measure contact angles.

Floating particles which should sink are held up by capillary forces at the line of contact of the three phases on the particle surface. The hanging depth between the contact line and the highest point on the meniscus depends on whether the meniscus attaches to the particle on the smooth surface with uniquely determined normal or at a corner or edge where the normal is undefined. Here we show that the hanging depth is determined by the position of the contact line on a floating sphere when the contact angle is fixed by the Young–Dupré law, and by the value of the contact angle which changes with the weight of the particle when the contact line is pinned at a sharp edge.

2.1. *Floating particles with sharp edges*

It is well known, but not well understood, that liquid–air–solid interfaces tend to locate at sharp edges. This mechanism allows a prismatic disk or cube to float with contact line pinned to its sharp rim. Even when a downward vertical force is applied by adding weights onto the top surface of a floating disk, as discussed below, the contact line remains pinned to the rim.

Obviously, a prismatic particle which is denser than the liquid below can float only if the vertical component of interfacial tension is sufficiently large to balance its buoyant weight and will sink when this is no longer true. The effects of the buoyant weight may be isolated in the case of a circular cylinder or disk, with axis vertical, which is suspended with the contact line on a circle perpendicular to the cylinder generator (see figure 3). The contact angle is fixed by the Young–Dupré law and does not change even as the contact line sinks due to change in the cylinder buoyant weight. The cylinder can be denser than the liquid provided that the vertical capillary force is just large enough to balance its buoyant weight. If the cylinder's weight is increased, it

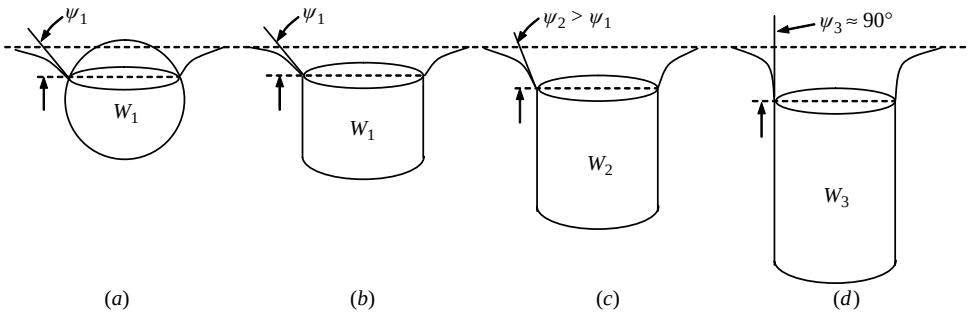

FIGURE 4. Effect of changing the buoyant weight on the contact angle at the rim of a cylinder. The contact angle is the same for a sphere (*a*) and disk (*b*) when the buoyant weights are the same. Increasing the buoyant weight leads to larger contact angles which have larger vertical components of the capillary force as shown in (*b*), (*c*) and (*d*). In the experiments of WBJ (2005) the cylinder would sink when $\psi \lesssim 90°$; however theoretically the cylinder can float with $\psi > 90°$ (Hesla & Joseph 2003).

will sink further and the contact line on the smooth surface will move upwards. But, the vertical component of capillary force will not change because the angle between the interface and the horizontal, which only depends on the contact angle, does not change when the cylinder sinks (see figure 3). Consequently, the maximum interfacial deformation, the vertical distance between the contact line and the highest point on the meniscus, will also not change as the cylinder sinks. The buoyancy force acting on the disk, however, increases, as it sinks into the liquid below. Disks of different weight in air, with same contact angle and buoyant weight can be suspended as in figure 3.

At a critical value of the disk weight, the contact line moves from the smooth surface to the sharp edge. If the disk weight is increased further, the contact line remains pinned at the sharp corner for a range of weights, even though the disk continues to sink further (see figures 4–7). A heavier-than-liquid disk can float with the interface pinned to the sharp edge, as in figure 4, provided the vertical component of the capillary force is large enough to balance its buoyant weight. In this paper, we will study the dynamics of floating disks in this state.

2.2. *Gibbs inequality*

This pinning of the contact line at the disk edge appears to be in conflict with the Young–Dupré law which states that the equilibrium contact angle between a liquid, a gas and a solid wall is constant

$$\gamma_{LG} \cos\alpha = \gamma_{SG} - \gamma_{SL},$$

where α is the contact angle and γ_{LG}, γ_{SG} and γ_{SL} are the interfacial energy between liquid and gas, solid and gas, and solid and liquid, respectively. To ensure that the equilibrium contact angle is fixed, when the interface at a small distance away from the contact line moves the contact line must also move. But, since the normal at the corner is not defined, the Young–Dupré law is not violated provided the contact angle α at the corner, as shown in figure 8, stays within the range specified by the Gibbs extension to the Young–Dupré law:

$$\alpha_0 < \alpha < 180 - \phi + \alpha_0$$

where ϕ is the wedge angle and α_0 is the equilibrium contact angle for the vertical face (see Gibbs 1906 and Princen 1969).

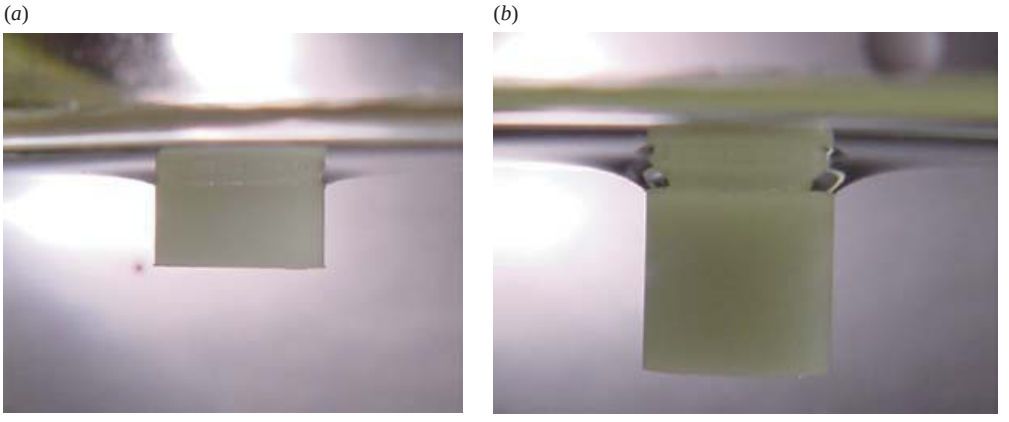

FIGURE 5. (From WBJ 2005). Two photos of floating Teflon disks of density $\rho_s = 1.4\,\mathrm{g\,cm^{-3}}$ held at the contact line in water of density $\rho_f = 1\,\mathrm{g\,cm^{-3}}$. Both disks have a diameter of 0.8 cm; the height from the bottom of the disk to the contact line is 0.4 cm in (*a*) and 0.8 cm in (*b*). The contact angle in (*b*) is larger than that in (*a*) in order to satisfy the force balance. The image of the disk projecting above the contact line is a reflection in the surface of the water.

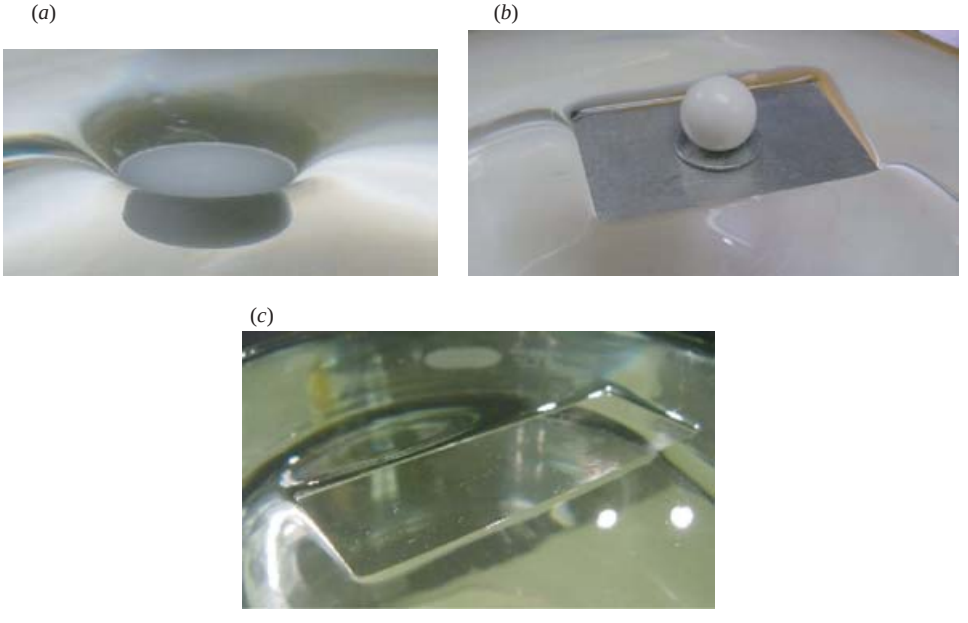

FIGURE 6. (From WBJ 2005). (*a*) The meniscus for a Teflon cylinder of density $\rho_s = 1.4\,\mathrm{g\,cm^{-3}}$ hanging from a flat edge in water. (*b*) An aluminum plate can float in water hanging from the sharp edge; when weighted by a Teflon ball, the plate still floats but the hanging depth increases. (*c*) A floating glass plate is held at the sharp edge in water. Spheres of aluminum and glass will sink in water, provided that the spheres are not so small that the surface tension will dominate the buoyant weight. The contact angle on the hydrophilic glass plate and the hydrophobic Teflon plate is determined by their buoyant weight and not by wettability.

2.3. *Vertical force balance in equilibrium*

An analysis of the forces which keep a sphere suspended in the interface between fluids was given first by Princen (1969), then by Rapacchietta & Neumann (1977),

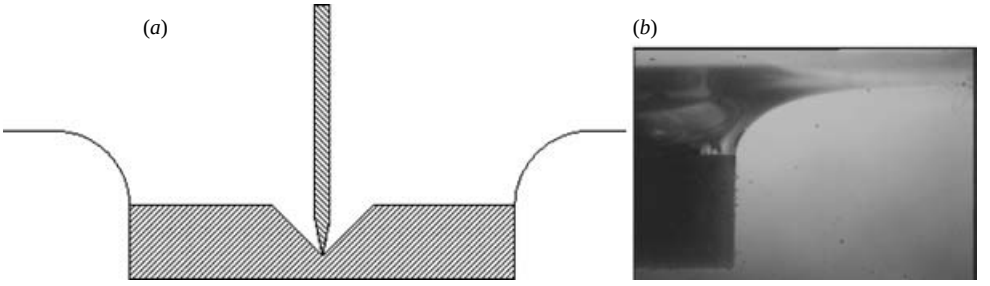

FIGURE 7. (From WBJ 2005). (*a*) A cartoon for the experiment determining the critical contact angle at the sharp edge. See § 2.5 for details of the experiment. (*b*) A photo from the video showing that the contact angle reaches 90° at a moment just before the disk sinks. The square, solid black part in the photo is the disk and the bright part is water.

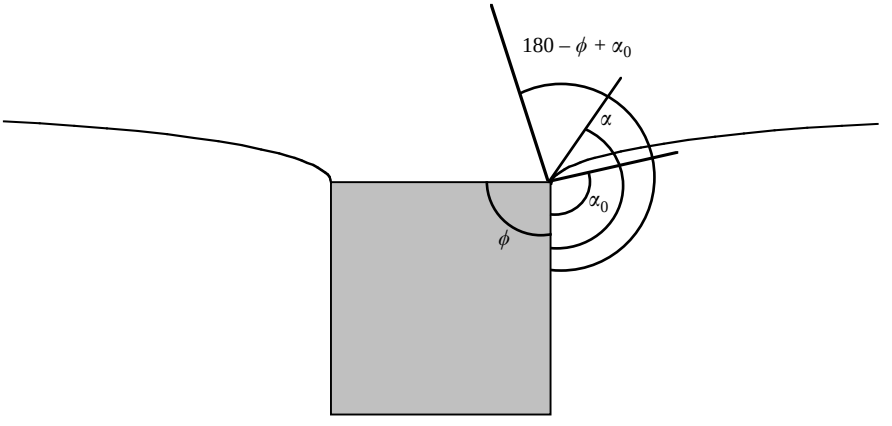

FIGURE 8. Two limiting angles for the Gibbs extension to the Young–Dupré law which states that the contact angle α at the sharp edge can take any value between α_0 and $180 - \phi + \alpha_0$.

and Katoh *et al.* (1992), who used the floating ball to measure contact angles. A detailed discussion of the vertical balance of a ball in equilibrium can be found in Joseph *et al.* (2003). An analysis of the forces which keep a heavy disk suspended in the interface at the sharp upper rim of the disk was given by Hesla & Joseph (2003), following an earlier analysis of Princen (1969) for a prismatic particle.

For equilibrium, the buoyant weight of the particle must be equal to the vertical component of the capillary force. If the particle density is larger than that of both fluids, equilibrium is possible only when the particle is hydrophobic and the vertical component of capillary force is large enough to balance its buoyant weight. The interface shape in this case is concave down and the net capillary force acts against gravity.

2.3.1. *Force balance for a sphere*

The conditions for equilibrium of a floating sphere can be framed with the help of the sketch in figure 9. The vertical component of capillary force F_c depends on the particle radius R, the surface tension coefficient γ, the filling angle θ_c and the contact angle α, and is given by

$$F_c = 2\pi(R\sin\theta_c)\gamma\sin[\theta_c - (\pi - \alpha)] = -2\pi(R\sin\theta_c)\gamma\sin(\theta_c + \alpha). \tag{2.1}$$

The above expression holds for both the hydrophobic and hydrophilic cases.

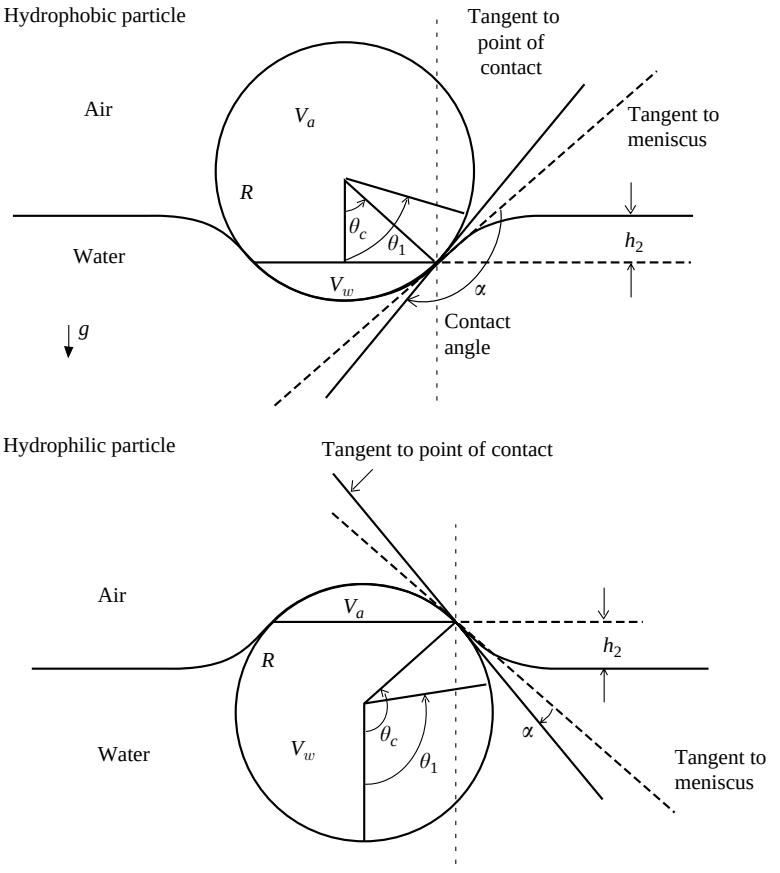

FIGURE 9. (From Joseph *et al.* 2003). Hydrophobic and hydrophilic particles in equilibrium. The position of the contact ring determines the angle θ_c. The point of extension of the flat meniscus on the sphere determines the angle θ_1. $h_2 = R(\cos\theta_c - \cos\theta_1)$.

The weight $M\boldsymbol{g}$ of a heavy particle in equilibrium is balanced by a capillary force $\boldsymbol{F}_c$ and net pressure force $\boldsymbol{F}_p$ satisfying:

$$\boldsymbol{F}_c + \boldsymbol{F}_p = M\boldsymbol{g}, \tag{2.2}$$

where F_c is given by (2.1). F_p is the pressure force given by

$$\begin{aligned} F_p &= \int_0^{\theta_c} p\cos\theta(2\pi R\,\sin\theta)R\,\mathrm{d}\theta \\ &= \rho_L g\pi R^3\left(\frac{2}{3} - \cos\theta_c + \frac{1}{3}\cos^3\theta_c\right) + \rho_a g\pi R^3\left(\frac{2}{3} + \cos\theta_c - \frac{1}{3}\cos^3\theta_c\right) \\ &\quad - (\rho_L - \rho_a)gh_2\pi R^2\sin^2\theta_c \end{aligned} \tag{2.3}$$

where h_2 is the meniscus height, and ρ_L is the density of the lower liquid and ρ_a is the air density. Substituting into (2.2) we obtain

$$\begin{aligned} &2\pi\gamma(R\sin\theta_c)\sin(\theta_c + \alpha) - \rho_L g\pi R^3\left(\frac{2}{3} - \cos\theta_c + \frac{1}{3}\cos^3\theta_c\right) \\ &\quad - \rho_a g\pi R^3\left(\frac{2}{3} + \cos\theta_c - \frac{1}{3}\cos^3\theta_c\right) + (\rho_L - \rho_a)gh_2\pi R^2\sin^2\theta_c = Mg \end{aligned} \tag{2.4}$$

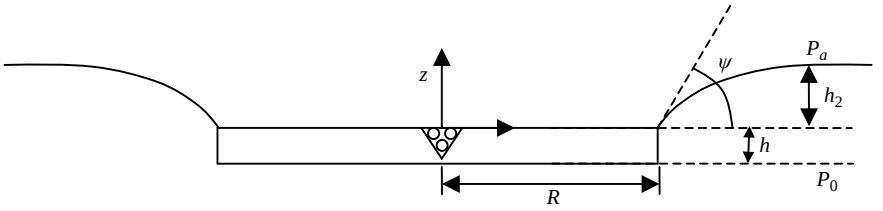

FIGURE 10. Heavier-than-liquid disk hanging from a flat edge. The capillary force is given by $F_c = 2\pi\gamma \sin\psi$, where γ is the interfacial tension. The meniscus is $z = h(r)$; $h(\infty) = h_2$ is the highest value of z on the meniscus. P_a is air pressure and P_0 is the pressure at the bottom of the disk $z = -h$. The disk may be weighted by heavy balls in the cone-shaped cavity, increasing h_2 and ψ without sinking.

with $M = \frac{4}{3}\pi R^3 g\rho_p$. Equation (2.4) may be expressed in a dimensionless form as

$$\sin\theta_c \sin(\theta_c + \alpha) = -\frac{1}{2}B\left[\frac{4}{3}l_1 - \left(\frac{2}{3} - \cos\theta_c + \frac{1}{3}\cos^3\theta_c\right)\right.$$
$$\left. - l_2\left(\frac{2}{3} + \cos\theta_c - \frac{1}{3}\cos^3\theta_c\right) + (1 - l_2)(\cos\theta_1 - \cos\theta_c)\sin^2\theta_c\right] \quad (2.5)$$

where $B = \rho_L R^2 g/\gamma$ is the Bond number and $l_1 = \rho_p/\rho_L$ and $l_2 = \rho_a/\rho_L$ are the density ratios.

The capillary force acts against gravity only when $\theta_c + \alpha - \pi$ is positive, in which case $\sin(\theta_c + \alpha) < 0$, otherwise it acts in the same direction as gravity. For example, if $\alpha = 3\pi/4$, a heavy sphere will float with $\theta_c > \pi/4$. For $\alpha = 3\pi/4$ and $\theta_c = \pi/4$, the force F_c is zero and there is no interface deformation. F_c increases when θ_c is increased from $\pi/4$, reaches its maximum value at $\theta_c \approx 1.9$ and then decreases with increasing θ_c. On the other hand, when the contact angle is π, F_c is always non-negative and its maximum value is for $\theta_c = \pi/2$, i.e. the sphere half immersed in the lower liquid. The buoyant weight of the particle also changes with θ_c.

2.3.2. *Force balance for a disk*

The force balance for the disk is given by (2.2). From figure 10 it is clear that

$$F_c = 2\pi R\gamma \sin\psi, \quad (2.6)$$
$$F_p = (P_0 - P_a)\pi R^2 = \rho_L g(h + h_2)\pi R^2. \quad (2.7)$$

Substituting into (2.2), we obtain

$$2\pi R\gamma \sin\psi + \rho_L g V + \pi R^2 h_2 \rho_L g = Mg, \quad (2.8)$$

where $V = \pi R^2 h$ is the volume of the disk. The angle $\psi = \alpha - 90$, where α is the contact angle, is measured from the horizontal. The dimensionless form of (2.8) is given by

$$\sin\psi = B\frac{1}{2}\left[(l_1 - 1)\frac{h}{R} - \frac{h_2}{R}\right]. \quad (2.9)$$

The meniscus height h_2 is determined from the solution of the meniscus equation

$$\rho g h[h(r) - h_2] = \frac{\gamma}{r}\left[\frac{rh'(r)}{\sqrt{1 + h'(r)^2}}\right]', \quad (2.10)$$

where the prime refers to the derivative with respect to r; the origin $(z, r) = (0, 0)$ is

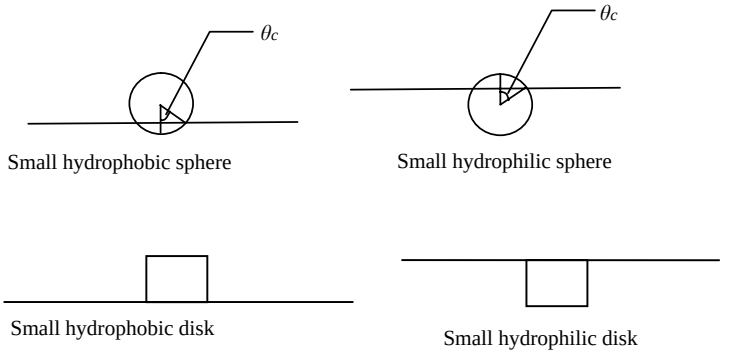

FIGURE 11. The deformation of the interface due to sufficiently small floating spheres or disks is negligible. A small hydrophobic sphere will float with $\theta_c \approx \pi - \alpha$ so that interfacial deformation is negligible even if it is denser than the liquid below. A small less dense hydrophilic sphere also does not deform the interface. Similarly, a small dense hydrophobic disk floats on the surface with negligible penetration into the liquid. A small hydrophilic disk which is lighter than the lower liquid does not deform the interface and it is kept inside the lower liquid by the capillary force which acts downwards.

in the plane at the centre of the circle of radius R defined by the contact line. The integration starts at $(z, r) = (0, R)$ where

$$h'(r) = \tan\psi. \tag{2.11}$$

Far from the particle, the meniscus is flat and

$$\lim_{r\to\infty}\{rh'(r), h(r)\} = \{0, h_2\}. \tag{2.12}$$

For a cylinder, the values of ψ and h_2 can be determined from the solution $z = h(r)$, using (2.8) together with

$$\rho g \int_R^\infty [h_2 - h(r)]r\,\mathrm{d}r = \gamma R \sin\psi \tag{2.13}$$

which follows from (2.9), (2.11) and (2.12).

Hesla & Joseph (2003) worked out an exact numerical solution of the problem just considered; they gave a simple mathematical argument that as the weight of a hydrophobic floating disk is gradually increased (figure 4), the maximum contact angle at the sharp rim which is attained before the disk sinks is greater than 90°. They presented numerical results which support this conclusion. Though such solutions are allowed by the equilibrium analysis, they have not been observed. It may be that configurations with contact angle greater than 90° are unstable (see figure 7).

2.4. *Small particles, large particles and heavy particles*

The left-hand side of equation (2.5), and thus also the right-hand side, lies in the range $-1 \leqslant \sin\theta_c \sin(\theta_c + \alpha) \leqslant 1$. Obviously, (2.5) cannot be solved if B is too large which may be the case when the sphere is too heavy or too large. Similarly, for a floating disk if B is too large, (2.9) cannot be solved; the disk will sink when the capillary force is not large enough to balance its buoyant weight.

As R approaches zero, the capillary force, which varies linearly with R, dominates the buoyant weight of the sphere which varies with R^3. In this limit since the Bond number $B = \rho_L R^2 g/\gamma \to 0$, the right-hand side of (2.5) is zero and thus $\sin(\alpha + \theta_c) \approx 0$ or $\theta_c \approx \pi - \alpha$ (see figure 11). We may therefore conclude that heavy small particles

m (g)	3.38	3.63	3.88	4.13	4.38
ψ (deg.)	28.4	37.8	43.0	51.7	71.1
H_2 (cm)	0.130	0.176	0.206	0.255	0.302
$2\pi R\gamma \sin\psi/mg$ (%)	5.27	6.31	6.58	7.11	8.08
$\rho_1 g h_2 \pi R^2/mg$ (%)	19.44	24.54	26.94	31.34	34.98
$\lvert e\rvert/mg$ (%)	1.03	0.01	1.8	0.77	0.36

TABLE 1. Quantities entering into the force balance equation (2.8). The residual e is computed from (2.14). The values of e are small. Taken from WBJ (2005).

can be suspended without causing significant interfacial deformation when B is small. Krahshesky *et al.* (1992, 1993) noted that for particles floating on water this limit is approximately reached when their diameter is 10 μm. Hence, the lateral capillary forces, which arise from interfacial deformation, are also insignificant when the particle diameter is smaller than 10 μm. Similarly, if volume of the disk approaches zero, the capillary force, which varies linearly with R, will dominate its buoyant weight which varies as hR^2. In this limit, the right-hand side of (2.8) is zero and $\sin\psi \approx 0$ or $\psi = 0$. The disk therefore does not deform the interface, and floats with its top surface in the plane of the interface (see figure 11).

The vertical component of the capillary force for the two positions in figure 3 can be zero only if the contact angle α is 90°. This implies that a small hydrophobic ($\alpha > 90°$) disk must float on its bottom edge, as shown in figure 10; it cannot be suspended as in figure 3. When the contact line is pinned to an edge the contact angle can take any value between the two values specified by the Gibbs inequality. The argument just given applies to all cases in which the Bond number is small, to particles with other shapes, like cubes and to lighter and larger particles.

When particles are partially immersed in a thin liquid film and their weight is supported by the substrate below, the arguments just given are not applicable and the interface deformation can be significant even for small particles. Kralchevsky & Nagayama (2000) have shown that in thin films the particle–particle attraction force increases with decreasing particle size.

2.5. *Experiments on floating disks pinned to the interface at the sharp edge*

Wang, Bai & Joseph (2005, referred to herein as WBJ) used a 3.38 g Teflon cylinder with a cone cut in the centre; 0.25 g steel beads were put in the cone to change the weight (see figure 10). The radius, height and volume of the disk are [1.27 cm, 0.495 cm, 2.51 cm^3]. The angle ψ and the depression h_2 were measured using a video camera. Measurements were taken at several azimuthal positions and the average values of ψ and h_2 recorded. After inserting the measured parameters into the force balance equation (2.8), the difference between the measured vertical force and the particle weight, the residual e, was computed:

$$e = Mg - 2\pi R\gamma \sin\psi - \rho_L g \pi R^2 (h + h_2). \tag{2.14}$$

Table 1 shows that the contact angle at the rim increases when the weight of the particle is increased. A maximum weight can be held in this manner; beyond this weight the particle will sink. WBJ did experiments to determine the critical contact angle corresponding to this maximum weight. The 3.38 g Teflon disk with a cone cut in the centre was used. The contact angle was gradually increased by pushing the disk down into the water with a needle (see figure 7). A video camera was used to record the whole process and the critical contact angle was determined using the

video replay. The contact angle increased up to 90° while the contact line was pinned at the rim (see figure 4); when the needle was pushed further down, the contact line moved away from the sharp edge to the flat top of the disk, and the disk sank instantaneously. They concluded that the critical contact angle corresponding to the maximum weight which could be held at the sharp edge is 90°. Hesla & Joseph (2003) have shown that the equilibrium solution for this problem allows contact angles larger than 90°; the vertical component of the capillary force decreases while the buoyant force increases, maintaining the balance. These larger contact angles may be unstable.

3. Motion due to the capillarity of floating particles on liquid surfaces

The deformation of a fluid–fluid interface due to floating or trapped particles gives rise to lateral capillary forces. A simple explanation is given in figure 3. A heavier-than-liquid particle will fall down a downward sloping meniscus while an upwardly buoyant particle will rise.

There are several ways to isolate the effects of capillarity from influence by gravity (see Joseph *et al.* 2003). Poynting & Thompson (1913) investigated the capillary effect by considering two vertical plates immersed in a liquid; the space between the plates is a two-dimensional capillary tube. If the plates are hydrophobic, the level in the capillary gap sinks below the liquid outside; if the plates are hydrophilic the levels will rise. Another way to take away the effects of gravity is to support the particles on a substrate. In this case, the horizontal forces are due to capillary effects alone. Katoh *et al.* (1992) studied the motion of a particle floating on a liquid meniscus surface which could be interpreted as motion on a substrate because the foaming phlystyrol particles used by them are an order of magnitude lighter than water, and thus minimize the effects of gravity compared to capillarity. Their experimental results are completely consistent with the predictions of Poynting & Thompson: when the sphere and the wall are alike with respect to wetting, say both are hydrophobic or hydrophilic, the wall and sphere attract; when they are unlike the sphere and wall repel.

There are only a few theoretical studies of capillary attraction. Nicolson (1949) was the first to derive an analytical expression for the capillary force between two floating bubbles by using the superposition approximation to solve the Laplace equation of capillarity. A similar approximate method was applied by Chan, Henry & White (1981) to floating spheres and horizontal cylinders. For horizontal cylinders alternative approaches were proposed by Gifford & Scriven (1971) and by Fortes (1982). The theoretical works are based on solutions of the Laplace equations for capillary menisci with translational or rotational symmetry, where the Laplace equation reduces to an ordinary differential equation. Saif (2002) developed an interesting analysis of the capillary interaction of long plates with round ends at prescribed heights which do not float.

For the case where the meniscus slope and the particle size are small, the Laplace equation for the interface shape was solved using bipolar coordinates by Krahshesky *et al.* (1992, 1993). This solution provides expressions for calculating the capillary meniscus force between two vertical disks, between two spheres partially immersed in a liquid layer and between a vertical disk and a sphere. Specifically, Kralchevsky & Nagayama (2000) have shown that the lateral force F_1 acting on particles of radii R_1 and R_2 separated by distance L is equal in magnitude and opposite in sign and is

given by

$$F_1 = -2\pi Q_1 Q_2 q K_1(qL)\left[1 + O\left(q^2 R_k^2\right)\right] \quad \text{when } L \gg r_k. \tag{3.1}$$

Here $r_k = R_k \sin(\theta_c)$, $k = 1, 2$ are the radii of the two contact lines as shown in figure 9 (where the particle radius is assumed to be R), $Q_k = r_k \sin\psi_k$, where ψ_k is the interface slope with the horizontal plane at the point of contact, $q = \sqrt{(\rho_1 - \rho_p)g/\gamma}$ is the inverse of the capillary length, and $K_1(x)$ is the modified Bessel function of the first order. Equation (3.1) is valid for particles much smaller than the capillary length. The force acting between two floating particles decreases with increasing distance between them.

The analysis just given is useful for determining the parameter values for which the particles can remain trapped on two-fluid interfaces, as well as the sign and magnitude of forces that act between two suspended particles, but to understand the actual motion of particles on the interface we must solve the governing equations of motion. Since the governing equations are complex, the dynamic behaviour of fluid and particles is not well understood.

A small number of theoretical studies have looked at the drag and diffusion coefficient of a spherical particle attached to a fluid interface (Brenner & Leal 1978, 1982; Goldman, Cox & Brenner 1967; Schneider, O'Neill & Brenner 1973; Majumdar, O'Neill & Brenner 1974; Wakiga 1957; Redoev, Nedjalkov & Djakovich 1992; Danov *et al.* 1995). Brenner & Leal have shown that the drag F_D acting on a floating sphere in the zero Reynolds number limit is $F_D = 3\pi\eta D U_x f_D$, where U_x is the lateral velocity of the sphere, D is the diameter, and f_D is the drag coefficient which is $O(1)$ and depends on the ratio of viscosities of the upper and lower fluids.

The only experimental study on determining drag coefficients of floating particles is by Petkov *et al.* (1995). They calculated the drag coefficients for particles of sub-millimetre radius by measuring the particle velocity under the action of a well-defined external force. They showed that the capillary interactions are quite strong and very long range. Danov *et al.* (1995) performed numerical simulations to obtain the drag coefficients for floating spheres, but they assumed that the interface between the two fluids stays flat and the particle translates with a constant velocity along the interface.

To understand the dynamics of clustering and self-assembly of particles due to capillarity, we have developed a numerical package which treats the problem by direct numerical simulation. The method is as exact as numerical methods allow; in particular, the changing shape of the meniscus and the hydrodynamic forces which move particles are computed and not modelled. At each time step, we solve the governing mass and momentum conservation equations for the two fluids, compute the forces acting on the particles and then move them using Newton's equations for rigid solids. The interface shape changes in response to the fluid motion while satisfying the contact angle or contact line requirement on the particle surface. In addition, across the interface the fluid properties change suddenly and a capillary force acts between the two fluids.

We have performed dynamic simulations of spherical particles for which the contact angle is maintained at the equilibrium value and the position of the contact line changes, as well as for floating disks with sharp edges. For floating disks, the meniscus remains pinned at the rim even when the disk moves relative to the interface, but the contact angle at the rim changes. In our numerical study it is assumed that the interface is initially flat and the top surface of the disk is in the plane of the interface. As the disk is denser than the liquid, it sinks but the contact line remains at the rim. Consequently, the interface near the rim becomes more vertical, increasing

the vertical component of the capillary force. In our code, the contact line is kept at the sharp edge of a floating cylindrical particle by making the level set function vanish on the rim.

In the next section we will state the governing equations for the fluids and the particles, briefly describe the level set and distributed Lagrange multiplier approaches and present our finite element method. A detailed description of the numerical method is included in the Appendix. In § 6, we will discuss a convergence study that shows that the numerical results are independent of the mesh size as well as the time step size and present results for the transient motion of particles along two-fluid interfaces.

4. Governing equations and dimensionless groups

In our numerical studies of particle motion in two-fluid interfaces we will assume that the fluids are immiscible and Newtonian. The particles are assumed to be rigid. Let us denote the domain containing the two liquids and N particles by Ω, the domain boundary by Γ_d, and the interior of the ith particle by $P_i(t)$. The governing mass and momentum conservation equations for the fluid phases can be written as

$$\rho\left[\frac{\partial \boldsymbol{u}}{\partial t} + \boldsymbol{u}\cdot\nabla\boldsymbol{u}\right] = \rho\boldsymbol{g} - \nabla p + \nabla\cdot\boldsymbol{\sigma} + \gamma\kappa\delta(\phi)\boldsymbol{n}; \quad \nabla\cdot\boldsymbol{u} = 0 \quad \text{in } \Omega\backslash\overline{P(t)}, \tag{4.1}$$

$$\boldsymbol{u} = \boldsymbol{u}_L \qquad \text{on } \Gamma_d, \tag{4.2}$$

$$\boldsymbol{u} = \boldsymbol{U} + \boldsymbol{\omega}\times\boldsymbol{r} \quad \text{on } \partial P(t), \tag{4.3}$$

with the extra stress tensor $\boldsymbol{\sigma} = 2\eta\boldsymbol{D}$, ρ is the fluid density which is different for the two fluids, p is the pressure, $\boldsymbol{D}$ is the symmetric part of the velocity gradient tensor, $\delta(.)$ is the Dirac delta function, $\boldsymbol{n}$ is the outer normal at the interface, γ is the surface tension, κ is the mean surface curvature, ϕ is the distance from the interface, η is the viscosity which is different for the two fluids and $\boldsymbol{u}_L$ is the prescribed velocity on Γ_d. The surface tension force acts along the interface between the two fluids.

The particle velocity $\boldsymbol{U}$ and angular velocity $\boldsymbol{\omega}$ are governed by

$$M\frac{\mathrm{d}\boldsymbol{U}}{\mathrm{d}t} = M\boldsymbol{g} + \boldsymbol{F}, \tag{4.4}$$

$$\frac{\mathrm{d}(\boldsymbol{I}_P\boldsymbol{\omega})}{\mathrm{d}t} = \boldsymbol{T}, \tag{4.5}$$

$$\boldsymbol{U}|_{t=0} = \boldsymbol{U}_0, \quad \boldsymbol{\omega}|_{t=0} = \boldsymbol{\omega}_0, \tag{4.6}$$

where M and $\boldsymbol{I}_P$ are the mass and moment of inertia of the particle. The particle density is denoted by ρ_P. The force $\boldsymbol{F}$ acting on a particle in the above equations is

$$\boldsymbol{F} = \oint(-p\boldsymbol{I} + \boldsymbol{\sigma})\cdot\boldsymbol{n}\,\mathrm{d}A + \oint_{CL}\boldsymbol{\Gamma}\,\mathrm{d}s \tag{4.7}$$

The first term on the right of (4.7) is the force on the particle due to stresses generated by fluid motion; the second term

$$\oint_{CL}\boldsymbol{\Gamma}\,\mathrm{d}s = \gamma\oint_{CL}\boldsymbol{n}_c\,\mathrm{d}s \tag{4.8}$$

is the capillary force, $\boldsymbol{\Gamma} = \gamma\boldsymbol{n}_c$ is a line stress on the contact line (CL) and $\boldsymbol{n}_c$ is the capillarity unit vector which lies in the interface and is normal to the contact line. This unit vector gives the direction of the action of the capillary force. A numerical algorithm for constructing $\boldsymbol{n}_c$ is given in § 5. Similarly, the torque $\boldsymbol{T}$ acting on the

particle is given by

$$\boldsymbol{T} = \oint (\boldsymbol{x} - \boldsymbol{X}) \times [(-p\boldsymbol{I} + \boldsymbol{\sigma}) \cdot \boldsymbol{n}] \, \mathrm{d}A + \oint_{CL} (\boldsymbol{x} - \boldsymbol{X}) \times \boldsymbol{\Gamma} \, \mathrm{d}s. \tag{4.9}$$

Here $\boldsymbol{X}$ is the centre of the particle, the first term gives the torque due to the fluid stress and the second that due to the capillary force acting on the contact line. For a spherical particle, which is one of the cases considered in this paper, if the interfacial tension γ is constant, the torque due to the interfacial tension is zero (see Singh & Hesla 2003).

The shape of the meniscus must be compatible with conditions which are prescribed at the contact line on every particle and at remote boundaries; for spherical particles the contact angle α is prescribed (see figure 9), but the contact line evolves during motion. For disks hanging at the sharp edge, the position of the contact line is prescribed and the contact angle changes. At remote boundaries different conditions could be considered, but in our simulations we have required the interface to be flat there. The motion of particles in fluid interfaces is very complex because the prescribed value of the contact angle is to be applied at the contact lines whose positions cannot be prescribed *a priori* and at the sharp edges the contact angle is not known *a priori*.

A particle placed in a two-fluid interface can be in a state of equilibrium provided its buoyant weight is equal to the z-component of the capillary force. The capillary force changes when the particle sinks or rises or the interface deforms to satisfy the contact angle requirement. Clearly, for a particle moving laterally along the interface, the vertical acceleration is small, and thus the z-component of (4.4) is

$$0 = -Mg + \boldsymbol{k} \cdot \oint (-p\boldsymbol{I} + \boldsymbol{\sigma}) \cdot \boldsymbol{n} \, \mathrm{d}A + \gamma \oint_{CL} \boldsymbol{k} \cdot \boldsymbol{n}_c \, \mathrm{d}s, \tag{4.10}$$

where $\boldsymbol{k}$ is the unit vector in the z-direction. The last term of (4.10) is the vertical projection of the capillary force which depends on the contact angles. For isolated spheres or disks in equilibrium (4.10) and the vertical projection of (4.1) with $\boldsymbol{u} = 0$ reduce to equation (2.5) or (2.8).

The x-component of the particle momentum equation, which governs its lateral motion, can be written as

$$M \frac{\mathrm{d}\boldsymbol{U}_x}{\mathrm{d}t} = \boldsymbol{i} \cdot \oint (-p\boldsymbol{I} + \boldsymbol{\sigma}) \cdot \boldsymbol{n} \, \mathrm{d}A + \gamma \oint_{CL} \boldsymbol{i} \cdot \boldsymbol{n}_c \, \mathrm{d}s, \tag{4.11}$$

where $\boldsymbol{i}$ is the unit vector in the x-direction. The first term on the right-hand side is the x-component of the fluid stress and the second is the x-projection of the integral of $\boldsymbol{n}_c$ around the contact line.

If we assume that a particle is accelerating slowly, which is the case, for example, when the two attracting particles are far from each other, then the two terms on the right-hand side of (4.11) balance each other. In the low Reynolds number limit, Brenner & Leal (1978) expressed the drag F_D acting on a sphere moving along the interface as

$$F_D = 3\pi\eta_L D U_x f_D \tag{4.12}$$

where f_D is the drag coefficient, which is of order one and depends on the viscosity ratio of the two fluids, the contact angle and the deformation of the interface which in turn depends on the density of the particle. Under these approximations, equations

(4.11) and (4.12) give

$$0 = 3\pi\eta_L D U_x f_D + \gamma \oint_{CL} \boldsymbol{i}\cdot\boldsymbol{n}_c \,\mathrm{d}s. \tag{4.13}$$

Equation (4.13) can be solved to obtain the lateral velocity U_x of the particles; U_x is proportional to γ/η_L, the 'capillary velocity' scale.

Petkov *et al.* (1995) used (4.13) for estimating the drag coefficient of floating spherical particles attracted by a plate. They measured U_x in an experiment and used the analytical expression for the horizontal force obtained by Kralchevsky *et al.* (1994) which is related to the integral term in (4.13). They found that the drag coefficient depends on the viscosities of the upper and lower fluid, as was shown by Brenner & Leal. The experimental values of the drag coefficient for several fluid–particle combinations were found to be of $O(1)$. The drag coefficient was greater than one for heavy particles, since they cause a greater deformation of the interface. They estimated the drag coefficients when the distance between the particle and the plate was greater than $35R$, where R is particle radius; for smaller distances (3.1) is not accurate because the inertial effects are not negligible. The estimate of the lateral capillary force they used is accurate only when the distance between the particle and the plate is large.

Danov *et al.* (1995) performed numerical simulations to study the dependence of the drag on a spherical particle translating in the interface on the ratio of viscosities. In their simulations, it is assumed that the interface between the two fluids is flat and the particle velocity is constant. They found that the agreement with experiments deteriorates with increasing particle density because interfacial deformation becomes not negligible.

In this paper we study problems for which inertial effects and time-dependent changes in the interface shape in response to particle motion are important. This happens to be the case when the distance between two floating particles is of the order of the particle radius because the interface shape changes continuously and the particles accelerate as they move toward each other.

The buoyant weight of particles is an important quantity in the description of the dynamics of capillary attraction. To see how it enters, we first remove the hydrostatic head from the pressure and write

$$\hat{p} = p + \rho g z. \tag{4.14}$$

In (4.1), the interface is given by

$$z = h(x, y, t). \tag{4.15}$$

The contact line can be specified by z_c, where h intersects the particle surface. Using (4.14), we find the pressure force acting on the particle

$$\oint p\,\boldsymbol{n}\,\mathrm{d}A = \oint (\hat{p} - \rho g z)\,\boldsymbol{n}\,\mathrm{d}A = \oint \hat{p}\boldsymbol{n}\,\mathrm{d}A - \rho_U V_U g - \rho_L V_L g, \tag{4.16}$$

where V_U is the volume of the particle above the contact line and V_L is the volume below and $M = \rho_P g(V_U + V_L)$. We may now write (4.4) as

$$M\frac{\mathrm{d}\boldsymbol{U}}{\mathrm{d}t} = [(\rho_P - \rho_U)V_U + (\rho_P - \rho_L)V_L]\,g\boldsymbol{k} + \oint (-\hat{p}\boldsymbol{I} + \boldsymbol{\sigma})\cdot\boldsymbol{n}\,\mathrm{d}A + \gamma \oint_{CL} \boldsymbol{n}_c\,\mathrm{d}s. \tag{4.17}$$

The first term on the right-hand side of (4.17) is only a portion of the buoyant weight (see equation (2.3)). For isolated spheres, with a prescribed contact angle, the contact line will be a circle on the sphere, so that the unknowns are V_U, V_L and $z_c = h(x, y, t)$.

For the disk hanging on the sharp rim, $V_U = 0$, $V_L = V$ and the contact angle ψ is unknown. Equation (4.5) can be written as

$$\frac{\mathrm{d}(\boldsymbol{I}_P\boldsymbol{\omega})}{\mathrm{d}t} = \oint (\boldsymbol{x}-\boldsymbol{X}) \times [((-\hat{p}+\rho g z)\boldsymbol{I}+\boldsymbol{\sigma})\cdot\boldsymbol{n}]\,\mathrm{d}A + \gamma \oint_{CL} (\boldsymbol{x}-\boldsymbol{X}) \times \boldsymbol{n}_c\,\mathrm{d}s. \quad (4.18)$$

The scaling parameters for equations (4.1)–(4.1), (4.17) and (4.18) are

$$[D, U, D/U, \eta_L U/D, U/D, \rho_L] = [\text{diameter, velocity, time, stress, angular velocity, density}]. \quad (4.19)$$

Here η_L and ρ_L are the viscosity and density of the lower liquid and $D = 2R$ is the diameter of the sphere or disk. The dimensionless equations are then in the form

$$l\left[\frac{\partial \boldsymbol{u}}{\partial t} + \boldsymbol{u}\cdot\nabla\boldsymbol{u}\right] = -\nabla\hat{p} + \frac{1}{Re}\nabla\cdot\boldsymbol{\sigma} + \frac{1}{We}\kappa\delta(\phi)\boldsymbol{n}; \quad \nabla\cdot\boldsymbol{u} = 0 \quad \text{in } \Omega\backslash\overline{P(t)}, \quad (4.20)$$

$$\frac{Re\, l_p}{\beta}\frac{\mathrm{d}\boldsymbol{U}}{\mathrm{d}t} = -GRe((l_P - l_U)V_U + (l_P - 1)V_L)\boldsymbol{k} + \oint(-\hat{p}\boldsymbol{I}+\boldsymbol{\sigma})\cdot\boldsymbol{n}\,\mathrm{d}S + \frac{1}{Ca}\oint_{CL}\boldsymbol{n}_c\,\mathrm{d}s, \quad (4.21)$$

$$\frac{Re\, l_p}{\beta}\frac{\mathrm{d}\boldsymbol{I}'_P\boldsymbol{\omega}}{\mathrm{d}t} = \oint (x-X)\times\left[\left(\left(-\hat{p}+\frac{\rho g z D}{\eta_L U}\right)\boldsymbol{I}+\boldsymbol{\sigma}\right)\cdot\boldsymbol{n}\right]\mathrm{d}s + \frac{1}{Ca}\oint_{CL}(\boldsymbol{x}-\boldsymbol{X})\times\boldsymbol{n}_c\,\mathrm{d}s, \quad (4.22)$$

where $\boldsymbol{k}$ is the unit vector along the z-direction. The particle mass $M = \rho_P D^3/\beta$, where $\beta = 6/\pi$ for a sphere and $\beta = 4D/\pi h$ for a disk with h being the disk height. The particle moment of inertia $\boldsymbol{I}_P = M\boldsymbol{I}'_P D^2$, where $\boldsymbol{I}'_P$ is the dimensionless moment of inertia. It can be shown that the term proportional to $\rho g z$ in (4.22) vanishes when the particle is a sphere, but does not vanish when the particle is a disk.

The dimensionless parameters which define the motion of particles are

$$[Re, G, Ca] = \left[\frac{\rho_L U D}{\eta_L}, \frac{gD}{U^2}, \frac{\eta_L U}{\gamma}\right] = [\text{Reynolds, gravity, capillary}]\ \text{numbers}, \quad (4.23)$$

the contact angle, and the property ratios are

$$[l, l_p, l_U, m] = \left[\frac{\rho}{\rho_L}, \frac{\rho_P}{\rho_L}, \frac{\rho_U}{\rho_L}, \frac{\eta_U}{\eta_L}\right] \quad (4.24)$$

where the subscript 'L' refers to the lower liquid and 'U' to the upper liquid. The density parameter l is equal to one in the lower liquid and in the upper fluid it is ρ_U/ρ_L and the Weber number $We = Re\,Ca$. In our numerical simulations, we use the dimensional equations (4.1)–(4.4), where the hydrostatic pressure variation is not removed from the pressure.

The selection of a characteristic velocity U for the definition of the dimensionless parameters in (4.19) is ambiguous since a characteristic velocity is not prescribed in the data. A natural choice for the velocity is the capillary velocity $U = \gamma/\eta_L$, which is suggested by other problems of motion driven by surface tension. With this choice we may compute

$$[Re, G, Ca] = \left[\frac{\rho_L \gamma D}{\eta_L^2}, \frac{g\eta_L^2 D}{\gamma^2}, 1\right] \quad (4.25)$$

from the prescribed data.

5. Numerical method

In this section we will briefly describe the key features of our numerical scheme. A detailed description of the numerical algorithm is included as an Appendix.

To perform direct numerical simulation of the motion of rigid particles trapped in a two-fluid interface, we must solve the governing mass and momentum conservation equations for the two fluids, compute the forces acting on the particles and then move them using Newton's equations (4.4). This is a difficult task because the interface shape changes as the particles move and the capillary force between the two fluids must be computed subject to the constraint that the contact angle is prescribed on a smooth surface and the contact line is prescribed on edges.

In this study we will assume that the dynamic contact angle is the same as the static contact angle. This enforcement of the contact angle on the particle surface causes the contact line to move in a way which may be described as a capillary-induced motion of the contact line due to a prescribed contact angle (see Friedrichs & Guceri 1993 and Sussman 2001 and references therein). At sharp edges, the motion of the particles is computed under the constraint that the interface remains pinned to the sharp edges of particles so that the contact angle changes as the motion proceeds. The contact angle can vary within the limits specified by the Gibbs extension of the Young–Dupré law.

In this work the level-set method is used to track the interface (see Osher & Sethian 1988; Sussman, Smereka & Osher 1994; Pillapakkam & Singh 2001; Sussman 2001). The level-set method works efficiently on a regular fixed grid and is compatible with the distributed Lagrange multiplier method (DLM) which will be used to track the motion of rigid particles (see Glowinski *et al.* 1999 and Singh *et al.* 2000). The DLM method also works efficiently on regular fixed grids. There are several other numerical approaches available for tracking the interface between two immiscible liquids, e.g. the surface tracking method (Unverdi & Tryggvason 1992), the volume of fluid method (Hirt & Nichols 1981), the moving grid methods (Glowinski *et al.* 1992) and the mapping method (Ryskin & Leal 1984), that can be used with the DLM method to study dynamics of floating particles.

In the level-set method, the interface position is not explicitly tracked, but is defined to be the zero level set of a smooth function ϕ, which is assumed to be the signed distance from the interface. In order to track the interface, the level-set function is advected according to the velocity field. One of the attractive features of this approach is that the method does not require any special treatment when a front splits into two or when two fronts merge.

The key idea in the level-set method is to advect ϕ with the local velocity, i.e.

$$\frac{\partial \phi}{\partial t} + \boldsymbol{u} \cdot \nabla \phi = 0. \tag{5.1}$$

As ϕ is a smooth function, it is relatively easy to numerically solve the above equation to update the interface position. In our implementation, it is assumed to be negative for the upper fluid, positive for the lower fluid and zero along the interface. The method also allows us to enforce the contact angle on the rigid particle surfaces and it is relatively easy to implement it in both two and three dimensions.

The motion of particles is tracked using a DLM method. One of its key features is that the fluid–particle system is treated implicitly by using a combined weak formulation where the forces and moments between the particles and fluid cancel, as they are internal to the combined system. The flow inside the particles is forced to be a rigid-body motion using the distributed Lagrange multiplier method. This

multiplier represents the additional body force per unit volume needed to maintain rigid-body motion inside the particle boundary, and is analogous to the pressure in incompressible fluid flow, whose gradient is the force needed to maintain the constraint of incompressibility.

In our numerical scheme the Marchuk–Yanenko operator splitting technique is used to decouple the difficulties associated with the incompressibility constraint, the nonlinear convection term, the rigid-body motion constraint and the interface motion. The operator-splitting gives rise to the following four sub-problems: an L^2 projection problem for the velocity and the pressure; a nonlinear advection–diffusion problem for the velocity; a distributed Lagrange multiplier problem that forces rigid-body motion within the particles; and an advection problem for the interface. Details of this method are set out in the Appendix.

5.1. *Reinitialization of* ϕ

The level-set function ϕ is reinitialized to be a distance function after each time step by solving the following equation obtained in Sussman *et al.* (1994) for the steady state

$$\frac{\partial \phi}{\partial t} + \boldsymbol{w} \cdot \nabla \phi = S(\phi_0) \tag{5.2}$$

where ϕ_0 is the distribution to be reinitialized and

$$\boldsymbol{w} = S(\phi_0)\frac{\nabla \phi}{|\nabla \phi|}.$$

Here $S(\phi_0)$ is the sign function, i.e. $S(\phi_0) = 1$ if $\phi_0 > 0$ and $S(\phi_0) = -1$ if $\phi_0 < 0$. In order to avoid discontinuities, in our code we use the following smoothed sign function:

$$S(\phi_0) = \frac{\phi_0}{\sqrt{\phi_0^2 + h_e^2}},$$

where h_e is equal to one and half times the element size. Equation (5.2) is a first-order hyperbolic partial differential equation which is solved using a positive only upwinding scheme described in Singh & Leal (1993). Clearly, the characteristics of (5.2) point in the direction of $\boldsymbol{w}$. Therefore, for the points inside the upper fluid $\boldsymbol{w}$ points upwards away from the interface and for the points inside the lower fluid it points downwards. Thus, (5.2) can be solved by specifying the boundary condition $\phi = \phi_0$ at the two-fluid interface $\phi = 0$.

5.2. *Variation of fluid properties across the interface*

In our finite element scheme the fluid viscosity is assumed to jump across the interface, i.e.

$$\eta = \begin{cases} \eta_L & \text{if } \phi > 0 \\ 0.5(\eta_L + \eta_U) & \text{if } \phi = 0 \\ \eta_U & \text{if } \phi < 0. \end{cases} \tag{5.3}$$

Here η_L and η_U are the viscosities of the lower and upper fluids, respectively. The fluid density, on the other hand, is assumed to vary smoothly across the interface

$$\rho = \begin{cases} \rho_L & \text{if } \phi > h_e \\ \rho_U & \text{if } \phi < -h_e \\ 0.5(\rho_L + \rho_U) + 0.5(\rho_U - \rho_L)\sin\left(\dfrac{\pi\phi}{2h_e}\right) & \text{otherwise,} \end{cases} \tag{5.4}$$

where h_e is equal to one and half times the element size, and ρ_L and ρ_U are the densities of the two fluids, respectively. This smoothing of the density is similar to that used by Sussman *et al.* (1994), and is needed for avoiding numerical instabilities when the density ratio ρ_L/ρ_U is large.

The surface tension force is smoothed and acts only on the elements for which ϕ is smaller than h_e. This is done by approximating $\delta(\phi)$ in (4.1) by a mollified delta function $\delta_{h_e}(\phi)$ using the approach described in Sussman *et al.* (1994):

$$\delta_{h_e}(\phi) = \begin{cases} \dfrac{1+\cos(\pi\phi/h_e)}{2h_e} & \text{for } |\phi| < h_e \\ 0 & \text{otherwise.} \end{cases} \tag{5.5}$$

The error introduced by smoothing of the surface tension force is $O(h_e)$. Equations (5.4) and (5.5) require that ϕ be maintained as a distance function, which we do in our implementation by reinitializing ϕ after each time step.

5.3. *Contact angle and contact line conditions*

The contact angle boundary condition on the particle surface, $\boldsymbol{n}\cdot\boldsymbol{n}_\phi = \cos\alpha$, where $\boldsymbol{n}$ is the unit outer normal on the particle surface and $\boldsymbol{n}_\phi = \nabla\phi/|\nabla\phi|$ is normal to the interface, is enforced using the approach described in Sussman (2001). Sussman used this approach to prescribe the contact angle on a stationary flat wall by extending ϕ to the 'outside' of the fluid domain. In this article the same approach is used to prescribe the contact angle of the two-fluid interface on the surface of a moving sphere. Let us define $\boldsymbol{t}$ and $\boldsymbol{n}_2$ as

$$\boldsymbol{t} = \frac{\boldsymbol{n}_\phi \times \boldsymbol{n}}{|\boldsymbol{n}_\phi \times \boldsymbol{n}|}, \quad \boldsymbol{n}_2 = \frac{\boldsymbol{t}\times\boldsymbol{n}}{|\boldsymbol{t}\times\boldsymbol{n}|}.$$

Notice that $\boldsymbol{t}$ is tangent to the contact line, and thus $\boldsymbol{n}_2$ is orthogonal to the contact line and lies in the tangent plane of the particle surface (see figure 12*a*). The next step is to construct a unit vector $\boldsymbol{u}_{ex}$ which is tangent to the interface with contact angle α, points inwards, and lies in the plane formed by $\boldsymbol{n}$ and $\boldsymbol{n}_2$; $\boldsymbol{n}_c = -\boldsymbol{u}_{ex}$ is the unit vector which gives the direction of the action of the capillary force. It is easy to verify that $\boldsymbol{u}_{ex}$ depends on $c = \boldsymbol{n}_\phi\cdot\boldsymbol{n}_2$ and is given by

$$\boldsymbol{u}_{ex} = \begin{cases} \dfrac{\boldsymbol{n}-\cot(\pi-\alpha)\boldsymbol{n}_2}{|\boldsymbol{n}-\cot(\pi-\alpha)\boldsymbol{n}_2|} & \text{if } c<0 \\ \dfrac{\boldsymbol{n}+\cot(\pi-\alpha)\boldsymbol{n}_2}{|\boldsymbol{n}+\cot(\pi-\alpha)\boldsymbol{n}_2|} & \text{if } c>0 \\ \boldsymbol{n} & \text{if } c=0. \end{cases} \tag{5.6}$$

To enforce the prescribed contact angle, ϕ is extended inside particles and on their surfaces by solving

$$\frac{\partial\phi}{\partial t} + \boldsymbol{u}_{ex}\cdot\nabla\phi = 0. \tag{5.7}$$

In other words, for all nodes inside and on the particle surface (5.7) is used to modify ϕ. The resulting extended level-set function satisfies the contact angle on the particle surface.

The contact line on the particle surface moves when the contact angle is enforced using (5.7). This could be called the capillary-induced motion of the contact line due to a prescribed contact angle. This approach has been used in many past numerical studies of problems involving moving contact lines (see Friedrichs & Guceri 1993 and

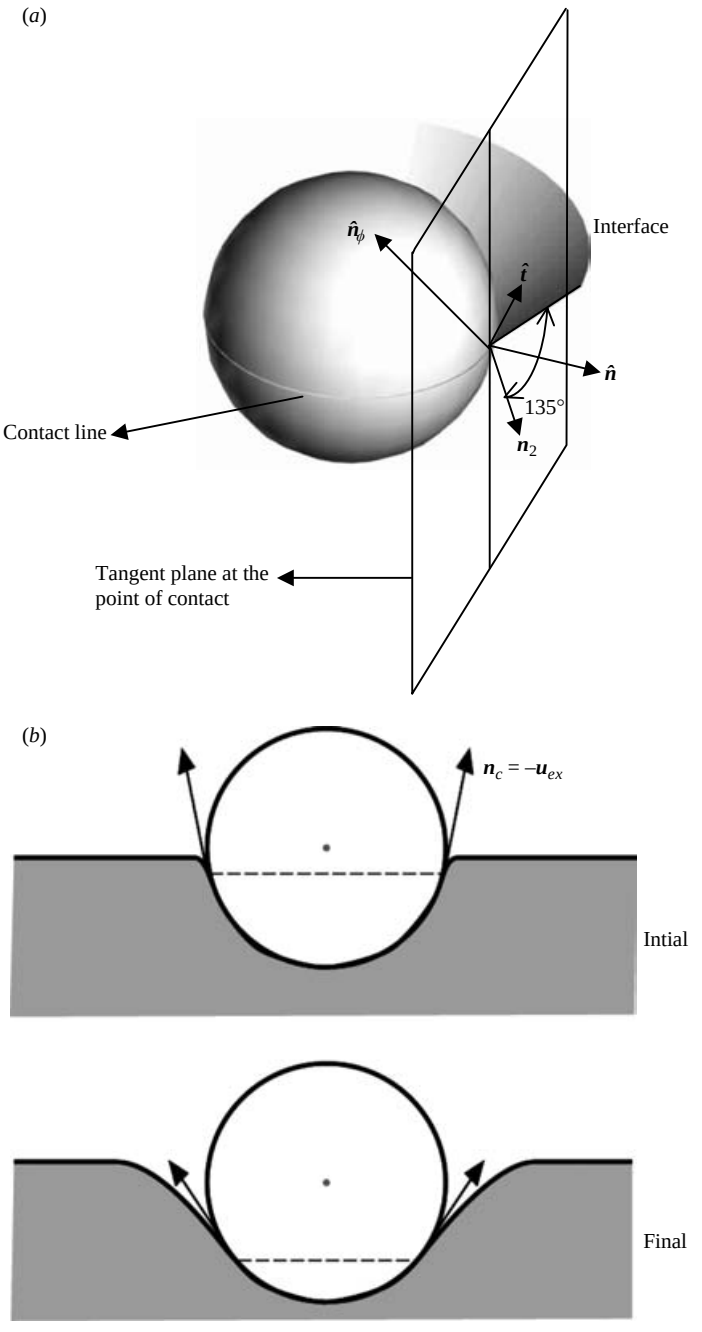

FIGURE 12. (*a*) The unit normal to the particle surface $\boldsymbol{n}$, the tangent to the contact line $\boldsymbol{t}$ and the normal to the interface $\boldsymbol{n}_\phi$ are shown. (*b*) A schematic of the interface shape and the contact line for the initial and steady states. In simulations the contact angle on the particle surface is prescribed to be 135° which is done by extending the level-set function to the inside of the particle. The contact line moves downwards because of the interface deformation near the particle and this decreases the vertical component of capillary force.

Sussman 2001 and references therein). For example, in injection moulding problems this approach has been used to track the motion of a liquid front advancing into empty moulds.

Clearly, this motion of the contact line on the particle surface is in conflict with the no-slip condition for viscous fluids (see Dussan V. & Davis 1974; Dussan V. 1976; Kistler & Scriven 1993 and references therein). However, if the contact line position on the particle surface is not updated, the contact line cannot move. In the capillary-induced-motion approach the no-slip condition is satisfied before and after the contact line moves; this pragmatic procedure could be called an effective numerical slip. This method of moving the contact line when the contact angle is prescribed has been used by Friedrichs & Guceri 1993 and Sussman 2001. An alternative approach used in some studies is to use a slip condition in a small neighbourhood of the contact line to ensure that it moves (see Kamal, Goyal & Chu 1988 and references therein). The slip velocity of the contact line is assumed to be proportional to the shear stress on the wall. This approach however does not ensure that the contact angle remains constant. Another aspect of the floating particle problem not treated here is that the contact angle for advancing and receding contact lines is different which can change the dynamical behaviour of floating particles.

6. Initial value problems for the evolution of floating particles to equilibrium

Here we report results of simulations of initial value problems for spheres and disks which are initially motionless, but not in equilibrium, to an equilibrium in which they are again motionless. The particles are heavier than the heavy liquid below and they float. Initially, the particles are motionless and imbedded in a flat interface; the spheres are centred with their midplane in the interface and the contact angle is fixed and held at 135° throughout the simulation. The assumed value of the contact angle is likely to be insensitive to the contact line speed in real experiments, as the contact angle is relatively large. Disks are pinned at the sharp edge of the upper rim throughout the simulation.

We do simulations for one sphere, one disk, two and four spheres and two disks. Initially, particles are not in equilibrium because they are heavy and must sink to equilibrium. For all cases, the particles reach an equilibrium in which they are motionless and in a balance between capillary forces and the buoyant weight; for single particles, spheres and disks, the computed values at equilibrium can be compared with the analytical expressions (2.5) and (2.8) and the agreement is satisfactory. The evolution to equilibrium for more than one particle takes place by sinking and capillary attraction; at the end the particles have self-assembled.

The conditions under which spheres and disks evolve to equilibrium are different. The interface near the spheres adjusts to meet the contact angle requirement and they sink until the buoyant weight becomes equal to the vertical component of the

FIGURE 13. The particle position and the interface shape and the velocity field in the domain midsection are shown. The length of velocity vectors is magnified 60 times and shown at every other node. The length of the velocity vectors in (*b*) (not shown) is smaller indicating that the fluid velocity decreases with time. The oblique and side views are shown. (*a*) $t = 0.003$. The fluid velocity is largest near the contact line where the interface curvature is large. (*b*) $t = 0.08$. The dimensionless parameters based on the maximum particle velocity are ($Re = 0.064$, $G = 1916.0$, $Ca = 0.02$) and based on the capillary velocity are ($Re = 3.2$, $G = 0.766$). After steady state is reached, the velocity is approximately zero everywhere in the domain.

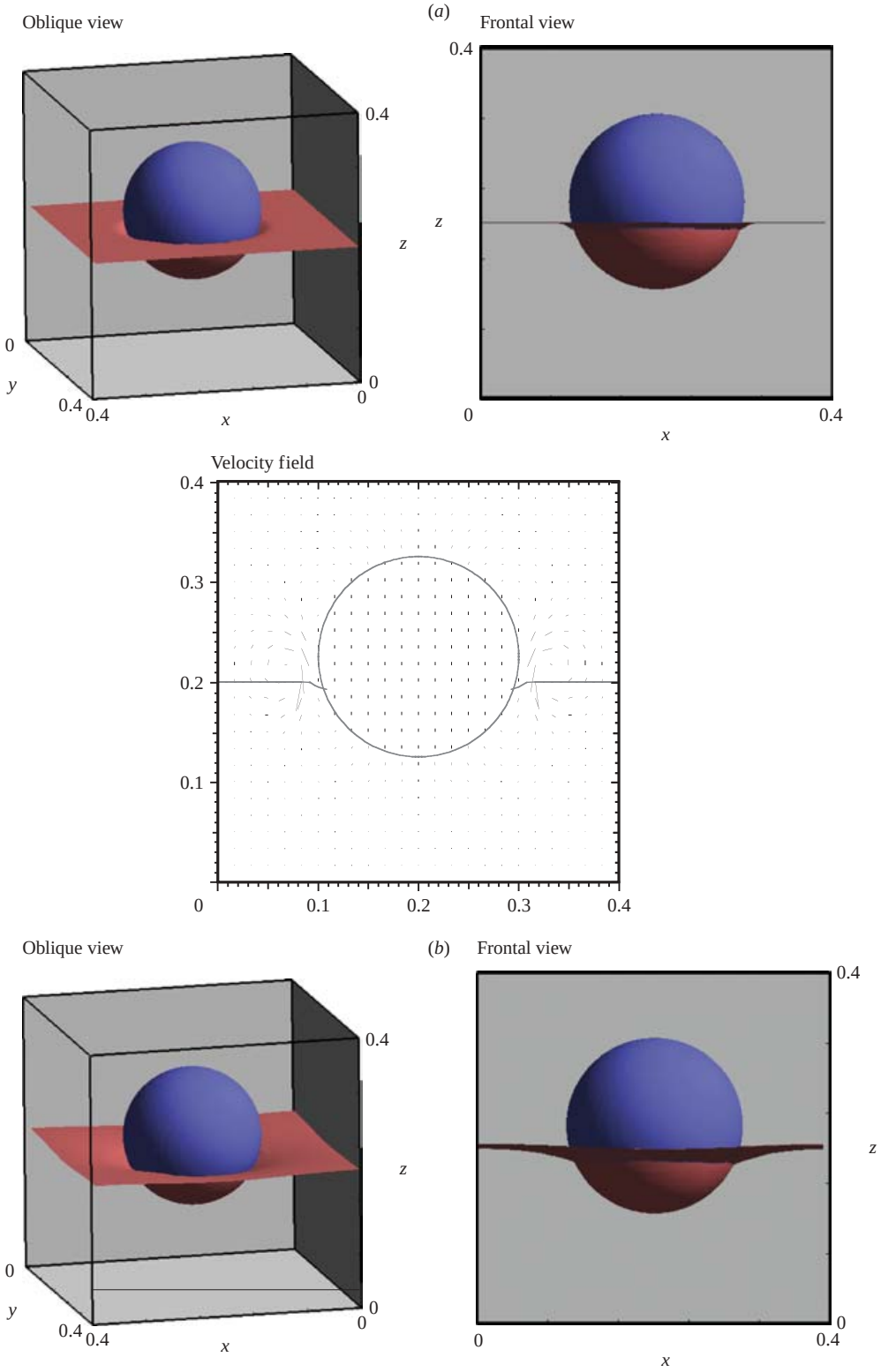

FIGURE 13. For caption see facing page.

capillary force. The disks, on the other hand, sink causing the interface to deform and increasing the contact angle and the vertical component of the capillary force. The disks stop sinking when the vertical component of the capillary force becomes equal to the buoyant weight.

An attractive force between floating particles arises because the meniscus between them drops in much the same way as a water meniscus will sink in a hydrophobic capillary tube. This dropping of the meniscus inside relative to the outside produces an asymmetry which generates attractive capillary forces. For spheres, since the contact angle is fixed, the contact line between the spheres drops. For disks, since the contact lines are fixed at the rim, the contact angles between the two disks decrease. In both cases, the asymmetry results in an attractive lateral capillary force acting on the particles.

The domains used in our simulations are box shaped with rectangular cross-sections. The coordinate system used throughout this paper is shown in figure 13. The x-, y- and z-components of particle velocity will be denoted by u, v and w, respectively.

We will also assume that all dimensional quantities, unless otherwise noted, are in the CGS units. The lower fluid density $\rho_L = 1.0\,\mathrm{g\,cm^{-3}}$. The viscosity of the lower fluid, and the density and viscosity of the upper fluid are varied. The particle density is assumed to be greater than one. The values of the interfacial tension are selected to ensure that the particle remains suspended in the interface. The acceleration due to gravity $g = 981.0\,\mathrm{cm\,s^{-2}}$ and acts along the negative z-direction. The initial velocities are assumed to be zero everywhere.

The no-slip boundary condition is applied on the surface of the box-shaped computational domains. The contact angle between the interface and the box boundaries is assumed to be 90°, the interface near the walls is flat.

We next present the results for floating spheres and disks, to demonstrate that the scheme works correctly, and that it reproduces the expected dynamical behaviour and the equilibrium state.

6.1. *Initial value problems for floating spheres*

In this subsection, we compute the motion of spheres released in the interface; the contact line intersects the sphere at a place different than that required for equilibrium.† The sphere diameter is assumed to be 0.2 cm. The initial interface shape is flat, except near the sphere surface where a contact angle of 135° is prescribed (see figure 12). The parameters are in the range for which a sphere trapped on the interface can be in equilibrium. The equilibrium interface shape and the floating height depend on the problem parameters.

6.1.1. *Motion of a single sphere*

When a sphere is suddenly released in the interface, the meniscus shape evolves to equilibrium. During this time, the velocity field in the two fluids is non-zero and the capillary force acting on the particle varies; the sphere velocity and its position in the interface change with time. The final equilibrium position described by analytical expression (2.5), however, is independent of these transients and can be used to verify the accuracy of numerical results.

† If the initial particle position was such that the interface did not touch the particle surface, then we would also need to address the problem of an interface coming in contact with a solid surface. This would require us to include additional physics to specify the conditions under which an interface can touch a solid surface. This physics is not included in the current version of our code.

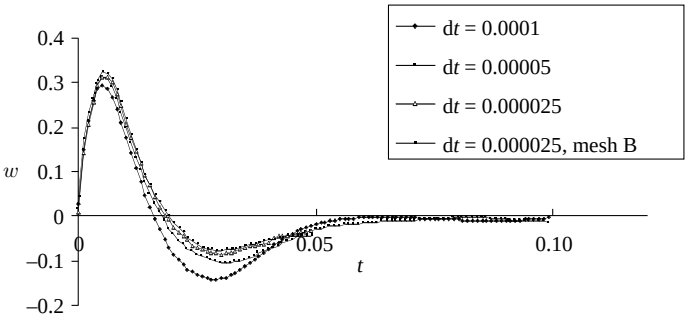

FIGURE 14. The vertical component of sphere velocity w released from rest on the interface is shown as a function of time for three different values of the time step. The curve marked mesh B is for a more refined mesh. The density and viscosity of the lower fluid are $1.0\,\mathrm{g\,cm^{-3}}$ and 1.0 P, and those of the upper fluid are $0.1\,\mathrm{g\,cm^{-3}}$ and 0.1 P. The interfacial tension is $16.0\,\mathrm{dyn\,cm^{-1}}$ and the particle density is $1.05\,\mathrm{g\,cm^{-3}}$.

We first present results that show that the trajectory of a sphere released in the two-fluid interface is independent of the mesh resolution and the time step. We have used two regular tetrahedral meshes to show that the results converge with mesh refinement. In a tetrahedral element there are seven velocity and four pressure nodes. The rigid-body constraint inside particles is enforced using uniformly distributed collocation points. The number of velocity nodes and elements in the first mesh are 117 649 and 13 824, respectively. In the second mesh, referred to as mesh B, there are 274 625 velocity nodes and 32 768 elements. The time step for these simulations is 0.0001, 0.00005 or 0.000025.

The sphere density is $1.05\,\mathrm{g\,cm^{-3}}$ and the interfacial tension is $16.0\,\mathrm{dyn\,cm^{-1}}$. The upper fluid density is $0.1\,\mathrm{g\,cm^{-3}}$ and the viscosity is 0.1 P. The initial velocity distribution in the fluid, and the sphere's linear and angular velocities are assumed to be zero. The domain is assumed to be cubical with sides 0.4 cm. The sphere centre is at a distance of 0.02 cm above the undeformed interface which passes though the domain centre.

In figure 14, w is plotted as a function of time for three time steps and two mesh resolutions. When the time step is reduced or when the mesh is refined the variation of w with time remains approximately the same. This allows us to conclude that the numerical results converge with both mesh and time step refinements.

Figure 14 shows that the vertical component of the sphere velocity w increases for $t \lesssim 0.005$ s and then it starts to decrease†; it becomes negative for $t \approx 0.019$ s and then increases again and becomes very small and fluctuates around zero for $t \gtrsim 0.06$ s. The other components of velocity u and v remain small for all times. We will assume that for $t = 0.06$ s the sphere has reached a state of equilibrium with $h_2 = 0.156R$ and

† Professor Howard Stone has suggested that the floating particle essentially behaves as a forced spring–mass system (gravity and surface tension, with the contact angle, enter as the original driving force for motion, and the density difference of the two fluids is like a spring), with damping provided by the fluid viscosity. Hence, one can derive a dimensionless ODE of the form $\mathrm{d}^2Z/\mathrm{d}T^2 + A\,\mathrm{d}Z/\mathrm{d}T + BZ = 1$, where Z is the scaled position, T is the dimensionless time, A is a coefficient that involves the fluid viscosity and B is the ratio of buoyancy to particle mass. The right-hand side is 1 because of the choice of length and time scales. In particular, he defined $z^*/L = (\frac{1}{2}(\rho_1 + \rho_2) - \rho_p)/(\rho_1 - \rho_2)$ and $T = t/t_c$, $Z = z/z^*$, where t_c is conveniently chosen to include surface tension and buoyancy that drives the original motion. Also, see the footnote in § 6.2.1.

γ (dyn cm^{-1})	h_2/R	$R\cos\theta_c$ (cm)	θ_c (deg.)	$F_p + F_c$ (g cm s^{-2})
10	0.237	0.257	75.00	4.33
14	0.173	0.376	67.95	4.35
16	0.156	0.419	65.26	4.35
20	0.130	0.466	62.28	4.36
25	0.114	0.514	59.07	4.33

TABLE 2. The interfacial deformation h_2/R, the floating height $R\cos\theta_c$ from numerical computation are used to compute the sum of the pressure and vertical component of capillary forces from (2.1) and (2.3) for 5 values of the interfacial tension. The sphere density is 1.05 g cm^{-3} and its weight is 4.315 g cm s^{-2}. The density of lower fluid is 1.0 g cm^{-3} and that of the upper fluid is 0.1 g cm^{-3}. For all five cases, $F_p + F_c$ is approximately equal to the particle weight; we get the correct value of the sphere weight from simulations. As expected, the sphere's floating height increases and the interface deformation decreases with increasing surface tension. The interfacial deformation for these calculations is restricted because the domain size is relatively small. But, we can still compare these values as the same domain is used for all interfacial tension values.

ρ_U (g cm^{-3})	h_2/R	$R\cos\theta_c$	θ_c (deg.)
0.1	0.156	0.419	65.26
0.01	0.159	0.417	65.34
0.0016	0.161	0.417	65.37

TABLE 3. The interfacial deformation h_2/R, the floating height $R\cos\theta_c$ and the point of contact θ_c are listed as a function of the upper fluid density. The interfacial tension is 16 dyn cm^{-1}. The sphere density is 1.05 g cm^{-3} and its weight is 4.315 g cm s^{-2}. The density of lower fluid is 1.0 g cm^{-3} and that of the upper fluid is varied. The floating height increases and the interface deformation decreases with decreasing density of the upper fluid.

$\theta_c = 65.26°$. The computed values given in table 2 are in good agreement with the equilibrium formula (2.5). We may therefore conclude that the state of equilibrium is captured correctly by our code. The dimensionless parameters based on the maximum vertical velocity are: $Re = 0.064$, $Ca = 0.02$, $G = 1916.0$ and $We = 1.28 \times 10^{-3}$.

To understand the initial increase in w, we notice that the angle θ_c giving the position of the contact line in figure 13(a) is larger than that for the equilibrium state shown in figure 13(b) (also see figure 12b). Thus, the vertical component of capillary force is initially larger than the final value and as a result the particle moves upwards. This is a consequence of the fact that initially the interface is approximately flat everywhere except near the sphere (see figure 13a). The large curvature of the interface near the sphere at early times is reduced by interfacial tension and the interface assumes its equilibrium shape. The contact line moves downwards, reducing the vertical component of the capillary force. The vertical component of the pressure force in figures 13(a) and 13(b) are different, but since in the case shown in figure 13(a) the fluid velocity is not small, the pressure force cannot be determined using hydrostatics.

To validate our code further, we performed calculations for five different values of interfacial tension γ while keeping the other parameters fixed. In table 2 we have listed the floating heights, defined to be the vertical distance of the particle centre from the contact line, and the sum of the pressure and vertical component of capillary forces acting on the particle for these five values of the interfacial tension. For all

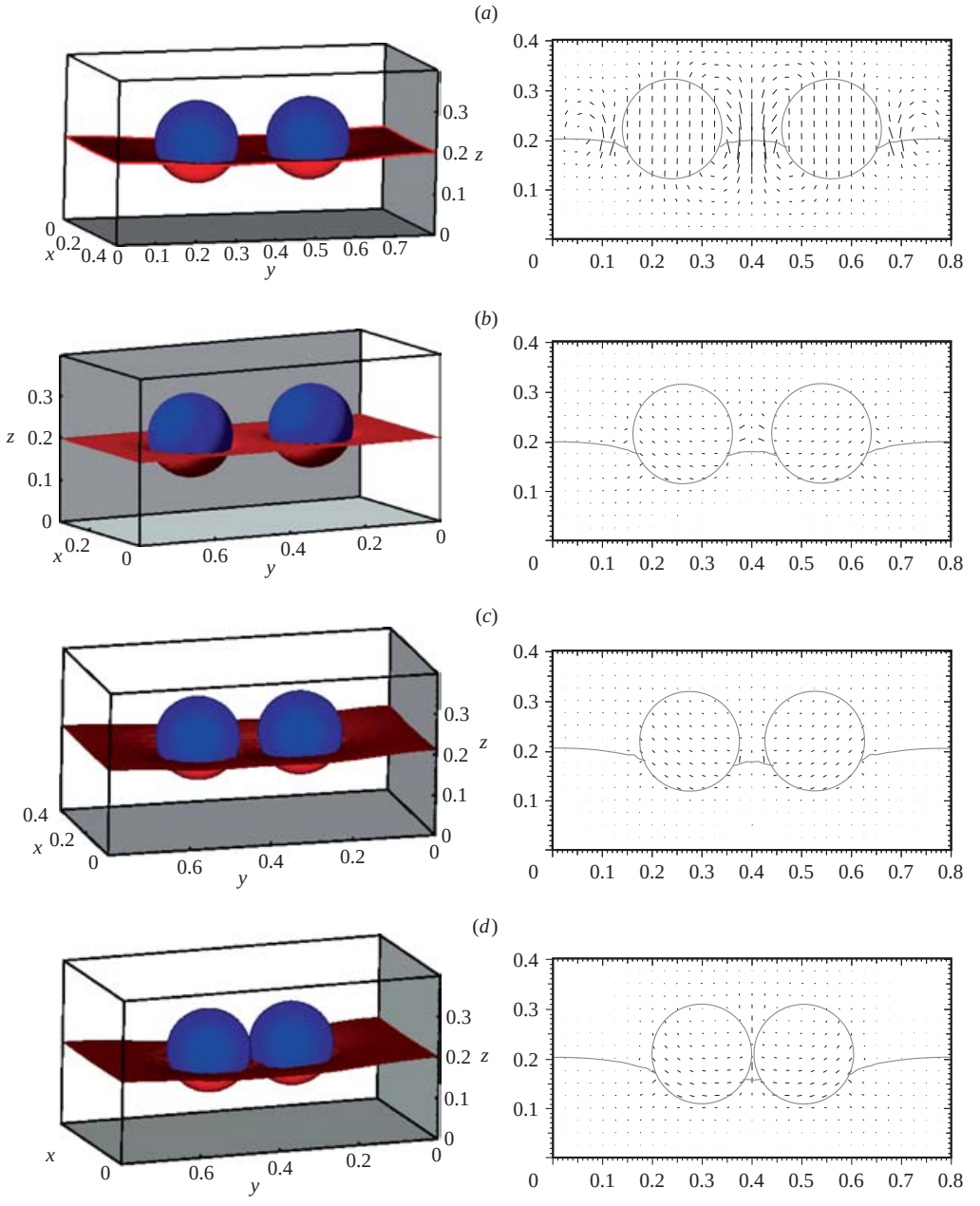

FIGURE 15. The positions of two spheres suspended in the two-fluid interface and the velocity distribution at the domain midsection are shown at $t = 0.0042$, 0.175, 0.225 and 0.339 (*a–d*). The length of velocity vectors is magnified 100 times and shown at every other node. The length of the velocity vectors is largest in (*a*) and smallest in (*d*) which indicates that the maximum velocity in the domain is decreasing with time. The particles are moving toward each other in the interface. The particles are 'supported' by the capillary force associated with the deformation of the interface. The surface tension is 16.0 dyn cm^{-1}, the particle density is 1.05 g cm^{-3} and the density of the top fluid is 0.01 g cm^{-3} and that on the bottom is 1.0 g cm^{-3}. The initial distance between the spheres is $3.2R$. The dimensionless parameters based on the maximum particle velocity are ($Re = 0.028$, $G = 1.0 \times 10^4$, $Ca = 0.00875$) and based on the capillary velocity are ($Re = 3.2$, $G = 0.766$).

cases in equilibrium, as required, $F_p + F_c$ is approximately equal to the particle's weight. There are small differences due to numerical errors.

In table 3 we have listed the floating heights for two additional cases where the density of the upper fluids are $0.01\,\mathrm{g\,cm^{-3}}$ and $0.0016\,\mathrm{g\,cm^{-3}}$, and the corresponding viscosities are 0.033 P and 0.0166 P. The interfacial tension is $16.0\,\mathrm{dyn\,cm^{-1}}$. The time step used for these calculations was 2×10^{-5} s. It is necessary to use a smaller value of the time step for these simulations because the ratio of lower and upper fluid densities is larger. The time step used is smaller also when the ratio of the lower and upper fluids viscosities is larger. The domain was discretized using mesh B described above. Table 3 shows that the floating height slightly decreases when the density of the upper fluid is reduced.

The equilibrium analysis, presented in § 2, assumes that the fluid extends to infinity in the x-, y- and z-directions which is not the case for our simulations. This may explain some differences between our simulations and the analytical results. These differences are expected to decrease with increasing box size. We also wish to note that for our simulations the magnitude of fluid velocity decreases as the state of equilibrium is approached, but it does not decrease beyond a certain value which depends on the fluid viscosity, surface tension and the interface curvature. The flow develops steady spurious circulation cells around the interface that are similar to those seen in simulations of drops (Scardovelli & Zaleski 1999). It has been noted by D. D. Joseph that these circulation cells arise in simulations because the discretized equation for the vorticity, which can be obtained by taking the curl of the momentum equation, contains a non-zero contribution from the layer (5.4) representing the delta-function in the level-set method. This creates vorticity along the discretized interface which diffuses into the domain. The presence of these cells, however, does not seem to affect the overall force balance, discussed in table 2, for equilibrium.

6.1.2. *Motion of two spheres*

We next present results for the case where two spherical particles are released near each other on the interface at the same vertical height. The initial interface position is assumed to be flat, except near the particle surfaces where a contact angle of 135° is prescribed. The initial vertical height of the spheres is higher than for a single sphere in equilibrium for the same parameter values. The parameters are assumed to be in the range for which a single sphere can be in equilibrium.

For these calculations, the particle density is $1.05\,\mathrm{g\,cm^{-3}}$. The interfacial tension is $16.0\,\mathrm{dyn\,cm^{-1}}$. The upper fluid density is $0.01\,\mathrm{g\,cm^{-3}}$ and viscosity is 0.033 P. The initial velocities are assumed to be zero. The domain height is 0.4 cm. The domain width in the x-direction is 0.4 cm and in the y-direction is 0.8 cm. The undeformed interface passes though the domain centre and the particle centres are initially at a height of 0.02 cm above the interface. The initial distance between the spheres in the y-direction is $2.6\,R$ or $3.2\,R$. The mesh resolution is comparable to that for the coarse mesh in § 6.1.1.

We have already noted that when two or more spheres released in the interface are close together they move towards each other due to the action of the lateral component of the capillary force associated with the asymmetric deformation of the interface around the particles. Figure 15(*a*) shows that for $t = 0.0042$ the interface shape is deformed in a small region around the spheres and farther away it is relatively flat; hence there is no lowering of interface. Consequently, at this time, the spheres do not experience any lateral attractive force. But, as for a single sphere, the interface height around the spheres decreases as time increases and, as a result, the contact

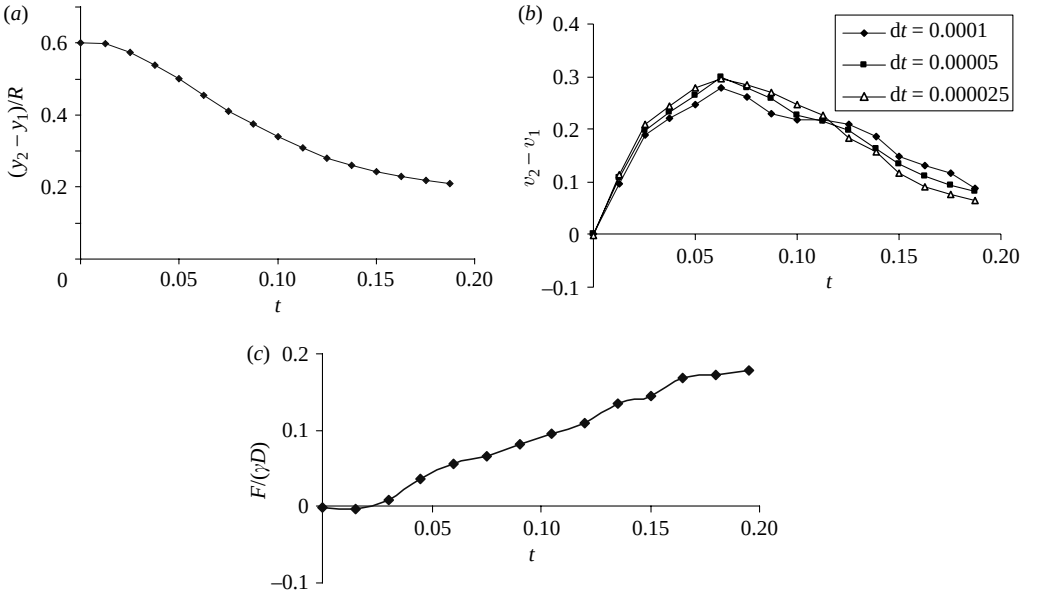

FIGURE 16. (*a*) The distance between the surfaces of spheres, (*b*) the approach velocity $v_2 - v_1$ and (*c*) the lateral capillary force are plotted as functions of time. The approach velocity $v_2 - v_1$ is shown for three different values of the time step. Notice that the approach velocity initially increases as the interface height between the spheres decreases and then decreases as the gap between the spheres becomes small. The initial distance between the spheres is $2.6R$.

lines on both spheres move downward. The vertical component of capillary force, which is initially larger than the final value, causes the spheres to move upward, but as the contact lines move downward the vertical capillary force decreases and the vertical velocities become negative. After this initial motion for $t \lesssim 0.05$ s, the vertical velocities become relatively small, but remain negative as the spheres approach each other. These initial transients in the velocities of the spheres could be diminished by setting their initial positions and interface shape closer to those for the equilibrium of an isolated sphere. This would however complicate the problem of prescribing initial conditions and make the problem less realistic.

Snapshots at $t = 0.0042$, 0.175, 0.225 and 0.399 of the evolution to equilibrium are shown in figure 15. At $t = 0.399$ the spheres are close to equilibrium.

The magnitude of the lateral capillary force $F/(\gamma D)$ increases as the distance between the spheres decreases, where F is the y-component of capillary force acting on a sphere (see figure 16). This is also seen as an increase in the approach velocity $v_2 - v_1$ plotted as a function of time in figure 16. However, the approach velocity begins to decrease due to the lubrication forces when the gap between the spheres is small enough. Simulations also show that when the distance between the spheres is larger, the initial approach velocity is smaller, because the lateral component of capillary force is smaller, and the time needed for the spheres to come together is larger. This is in agreement with (2.17) which implies that the lateral force increases with decreasing distance between the spheres. The dimensionless parameters based on the maximum lateral velocity are ($Re = 0.028$, $G = 1.0 \times 10^4$, $Ca = 0.00875$).

The contact line and the interface shape evolve as the spheres move toward each other. Therefore, the lateral component of the capillary force and the contribution of

d (cm)	$R\cos\theta_c$ (cm)	θ_c (deg.)	h_2/R
0.279	0.397	66.60	0.234
0.2493	0.388	67.13	0.289
0.2118	0.375	67.99	0.302

TABLE 4. The floating height $R\cos\theta_c$, the point of contact θ_c and the interfacial deformation h_2/R are shown as a function of the distance d between the spheres. The interfacial tension is 16.0 dyn cm^{-1}. The sphere density is 1.05 g cm^{-3}. The density of the lower fluid is 1.0 g cm^{-3} and that of the upper fluid is 0.1 g cm^{-3}. The floating height is computed based on the contact line position on the sphere surface away from the gap. Notice that the floating height of the spheres decreases and the interfacial deformation increases as they come closer. These values should approach the values for an isolated particle when the distance d is large.

the pressure to the force change as the distance between the spheres decreases. Petkov *et al.* (1995) measured the approach velocity of particles and found that when the gap between the particles is smaller than $O(30R)$, which is the case for our simulations, the nonlinearity of the interface curvature also influences the approach velocity. For the case described in figure 15 the simulations were stopped at $t = 0.339$ when the distance between the spheres' surfaces was reduced to $0.047R$. The interface shape at this time is shown in figure 15(d). Notice that the interface height between the spheres in this figure is even lower and the interface shape is flatter. For the case where the initial distance between the spheres' surfaces is $0.6R$ the time taken to reach the same separation is $\sim$0.181. The approach velocity remains relatively small for $t \lesssim 0.04$ during which the initial interfacial deformation takes place, which is approximately the time interval in which a single sphere reached equilibrium in § 6.1.1.

In figure 17 the approach velocity and the dimensionless distance between the spheres are shown for five additional parameter values. For these cases, the sphere centres are initially at a height of 0.04 cm above the interface and the initial distance between the spheres in the y-direction is $3.2R$. These figures show that the approach velocity becomes positive after a short time interval and increases as the spheres move toward each other. The approach velocity decreases when the gap between the spheres becomes small due to the lubrication forces. The lateral velocity for small times is negative because when the spheres sink into the lower liquid the hydrodynamic force is repulsive. From these figures we also conclude that the approach velocity increases when the viscosity of the upper or lower liquid is decreased. It also increases when the particle density or the surface tension coefficient is increased. The lateral velocity contains oscillations when the Reynolds number is of order one or larger.

Another interesting consequence of the lowering of interface height and contact lines between the spheres is a decrease in the vertical component of capillary force. This component of the capillary force acts against gravity and keeps them floating even though they are heavier than both liquids. This decrease causes the floating height of the spheres to decrease slightly (see table 4). For example, the height for a single sphere in § 6.1.1 for the same parameters was 0.419, but for the two spheres in figure 15(d) it is 0.375, where they are almost touching. This decrease in the floating height raises the contact line position everywhere except between the spheres so that the vertical component of the capillary force returns to the value required for balancing their buoyant weights (see figure 18). When the parameters are such that the sum of the vertical component of the capillary and pressure forces is near its maximum value for an isolated sphere, a decrease in the floating height would

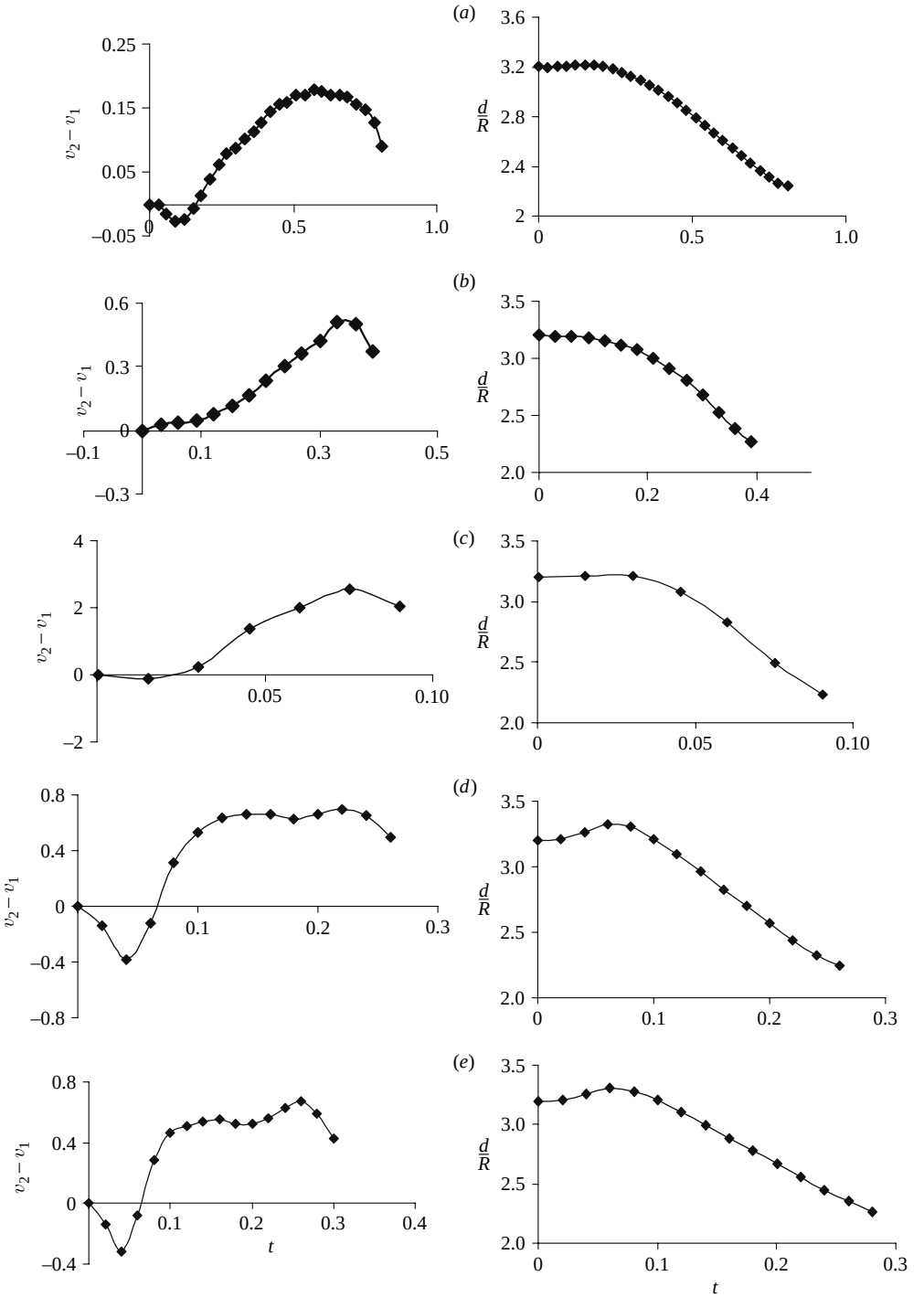

FIGURE 17. For caption see next page.

actually decrease the vertical component of total force. Therefore, if the spheres are barely floating, a decrease in the floating height will cause them to sink. This suggests that the clusters of spheres are more likely to sink than an isolated sphere.

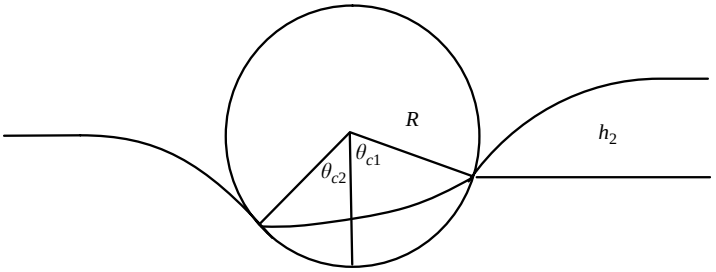

FIGURE 18. The contact line and the interface shape near a floating sphere. The contact line position on the left is lower, i.e. $\theta_{c2} < \theta_{c1}$, as there is another sphere floating to the left (not shown). Equation (2.1) implies that the vertical capillary force increases with increasing θ_c only when θ_c is less than 109° (which depends on the contact angle). Thus, the vertical capillary force acting on the right side of the sphere is larger than on the left side. But, if θ_{c1} is greater than 109°, this may not be the case.

6.1.3. *Motion of four spheres*

For these calculations the sphere density is $1.05\,\mathrm{g\,cm^{-3}}$ and the interfacial tension is $16.0\,\mathrm{dyn\,cm^{-1}}$. The upper fluid density is $0.1\,\mathrm{g\,cm^{-3}}$ and the viscosity is 0.1 P. The motion starts from rest. The domain height is 0.4 cm. The width along the x-direction is 0.8 cm and along the y-direction is 0.8 cm. The undeformed interface passes though the domain centre. The initial positions of the four spheres are (0.4,0.22,0.22), (0.4,0.58,0.22), (0.23,0.4,0.22) and (0.57,0.4,0.22). The mesh resolution is the same as for the coarse mesh in § 6.1.1.

After initial transients have died out, the spheres move toward each other. Their vertical velocity becomes small at $t \approx 0.05$ and around this time the interface height between the spheres begins to decrease.

In figures 19(a) and 19(b) the spheres and interface shape are shown at $t = 0.002$ and 0.096, respectively. In the first figure, the interface shape between spheres is not significantly deformed and the lateral velocities are small and in the second figure the interface between the spheres is lowered. The interface shape and the contact lines for the spheres are no longer symmetric and thus the lateral component of capillary

FIGURE 17. The distance between the spheres and the approach velocity $v_2 - v_1$ are plotted as functions of time. Notice that the approach velocity initially increases as the interface height between the spheres decreases and then decreases as the gap between the spheres becomes small. The initial distance between the spheres is $3.2R$. (a) The parameters are: ($l_p = 1.1, l_U = 1.0, m = 1.0$), $\eta_L = 0.1$ P and $\gamma = 2.0\,\mathrm{dyn\,cm^{-1}}$. The dimensionless parameters based on the maximum particle velocity are ($Re = 0.38$, $G = 5.4 \times 10^3$, $Ca = 0.0095$) and based on the capillary velocity are ($Re = 40.0$, $G = 0.491$). (b) The parameters are: ($l_p = 1.1, l_U = 1.0, m = 1.0$), $\eta_L = 0.01$ P and $\gamma = 2.0\,\mathrm{dyn\,cm^{-1}}$. The dimensionless parameters based on the maximum particle velocity are ($Re = 10.2$, $G = 784.8$, $Ca = 0.0025$) and based on the capillary velocity are ($Re = 4000$, $G = 4.9 \times 10^{-3}$). (c) The parameters are: ($l_p = 1.01, l_U = 10.0, m = 10.0$), $\eta_L = 0.1$ P and $\gamma = 16.0\,\mathrm{dyn\,cm^{-1}}$. The dimensionless parameters based on the maximum particle velocity are ($Re = 5.12$, $G = 29.9$, $Ca = 0.016$) and based on the capillary velocity are ($Re = 320$, $G = 7.66 \times 10^{-3}$). (d) The parameters are: ($l_p = 1.005, l_U = 2.0, m = 2.0$), $\eta_L = 0.1$ P and $\gamma = 4.0\,\mathrm{dyn\,cm^{-1}}$. The dimensionless parameters based on the maximum particle velocity are ($Re = 1.38$, $G = 412.1$, $Ca = 0.017$) and based on the capillary velocity are ($Re = 80$, $G = 0.12$). (e) The parameters are: ($l_p = 1.005, l_U = 2.0, m = 1.0$), $\eta_L = 0.1$ P and $\gamma = 4.0\,\mathrm{dyn\,cm^{-1}}$. The dimensionless parameters based on the maximum particle velocity are ($Re = 1.26$, $G = 496.3$, $Ca = 0.016$) and based on the capillary velocity are ($Re = 80$, $G = 0.12$).

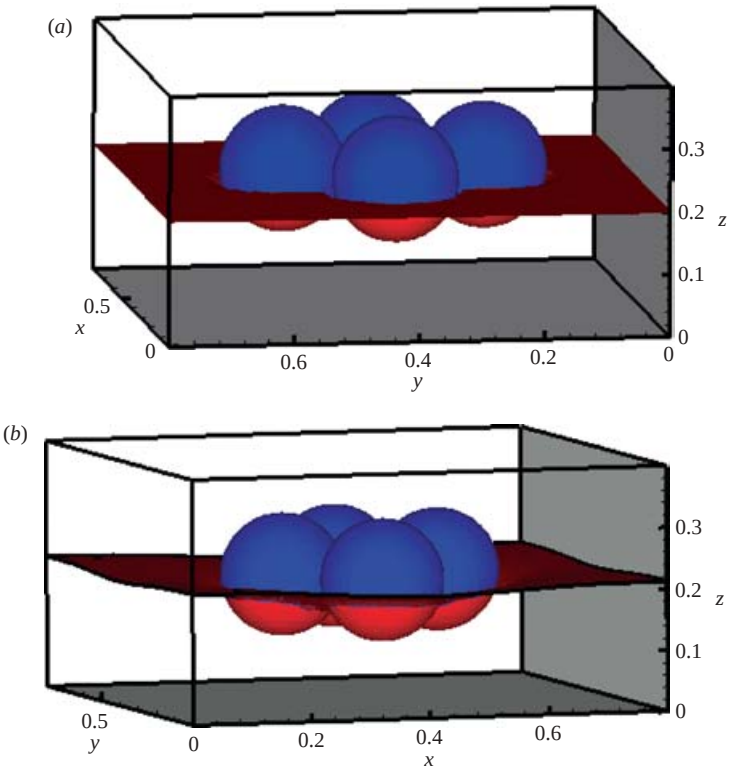

FIGURE 19. Oblique views showing the positions of four rigid spheres suspended in the two-fluid interface at (*a*) $t = 0.002$ and (*b*) 0.096. After they are released, they move toward each other. The surface tension is 16.0 dyn cm^{-1}, the particle density is 1.05 g cm^{-3} and the density of the top fluid is 0.1 g cm^{-3} and that on the bottom is 1.0 g cm^{-3}. The dimensionless parameters based on the maximum particle velocity are ($Re = 0.032$, $G = 7664.1$, $Ca = 0.01$) and based on the capillary velocity are ($Re = 3.2$, $G = 0.766$).

force acting on the spheres is not zero which causes them to move laterally towards each other.

As spheres approach each other, the vertical component of capillary force decreases due to the lowering of interface height between the spheres and thus the floating heights of the spheres decrease slightly (see figure 19*b*). For example, the height for a single sphere in § 3.1 for the same parameters is 0.419, for the two-sphere case it is 0.375, and for the four spheres in figure 19(*b*), where they are almost touching, it is 0.355.

6.2. *Initial value problems for floating disks*

The disks in our simulations are released with the top plane of the disk in the plane of the undeformed interface. The disk velocity, its position and the interfacial deformation change with time. The final state, described by expression (2.8), is independent of these transients and can be used to verify the accuracy of numerical results. In equilibrium, the interface shape is such that the capillary force is exactly balanced by a jump in the pressure across the interface and therefore no fluid flow is induced. The fluid velocity in simulations is small but non-zero.

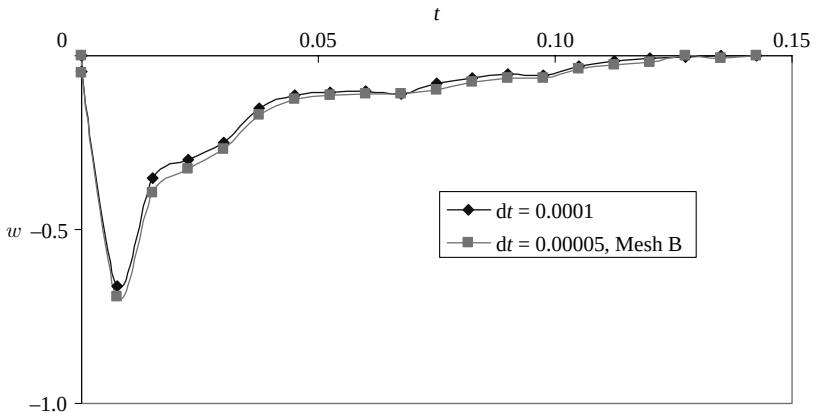

FIGURE 20. The vertical component of velocity w for a disk released in the interface is shown as a function of time for two different values of the time step. The curve marked mesh B is for a more refined mesh. The density and viscosity of the lower fluid are $1.0\,\mathrm{g\,cm^{-3}}$ and 1.0 P and those of the upper fluid are $0.1\,\mathrm{g\,cm^{-3}}$ and 0.1 P. The interfacial tension is $5.0\,\mathrm{dyn\,cm^{-1}}$ and the particle density is $1.5\,\mathrm{g\,cm^{-3}}$. The dimensionless parameters based on the maximum vertical velocity of the disk are ($Re = 0.35$, $G = 100.2$, $Ca = 0.014$) and based on the capillary velocity are ($Re = 50$, $G = 0.039$).

6.2.1. *Motion of a single disk*

We first discuss results that show that the trajectory of a disk released in the two-fluid interface is independent of the mesh resolution and the time step (see figure 20). We have used two regular tetrahedral meshes to show that the results converge with mesh refinement. The rigid-body constraint inside particles is enforced using uniformly distributed collocation points. The number of velocity nodes and elements in the first mesh is 117 649 and 13 824, respectively. In the second mesh, referred to as mesh B, there are 274 625 velocity nodes and 32 768 elements. The time step for these simulations is 0.0001 s or 0.00005 s.

The disk radius is 0.1 cm and its density is $1.5\,\mathrm{g\,cm^{-3}}$. The interfacial tension is $5.0\,\mathrm{dyn\,cm^{-1}}$. The density of the upper fluid is $0.1\,\mathrm{g\,cm^{-3}}$ and its viscosity is 0.1 P. Initially, all velocities are zero. The domain is cubical with sides 0.4 cm. The top surface of the disk is in the plane of the undeformed interface which is at $z = 0.28$ cm. The parameters are in the range for which a disk trapped in the interface can be in equilibrium.

The vertical velocity w shown in figure 20 decreases initially with time because the disk is denser than the liquid below and the vertical component of the capillary force is zero, as the interface is not deformed.† The buoyant weight and the contact angle increase simultaneously as the disk sinks (see figure 21).

We performed calculations for two additional values of the disk density ρ_p while keeping the other parameters fixed. Figure 22 shows that heavier disks sink to a

† Professor Howard Stone has shown that the coefficients of his ODE model described in the footnote of § 6.1 can be evaluated by assuming that L is equal to the disk radius and the viscous friction is given by the Stokes drag law. For the physical parameters of this problem, he finds that $A = 1/2$ and $B = 1/2$, approximately. The analytical solution of the ODE with these values looks almost identical in form to the numerical solution of figure 20. This model, based on physical arguments, therefore illustrates that some aspects of these systems can be quantitatively studied with simple models.

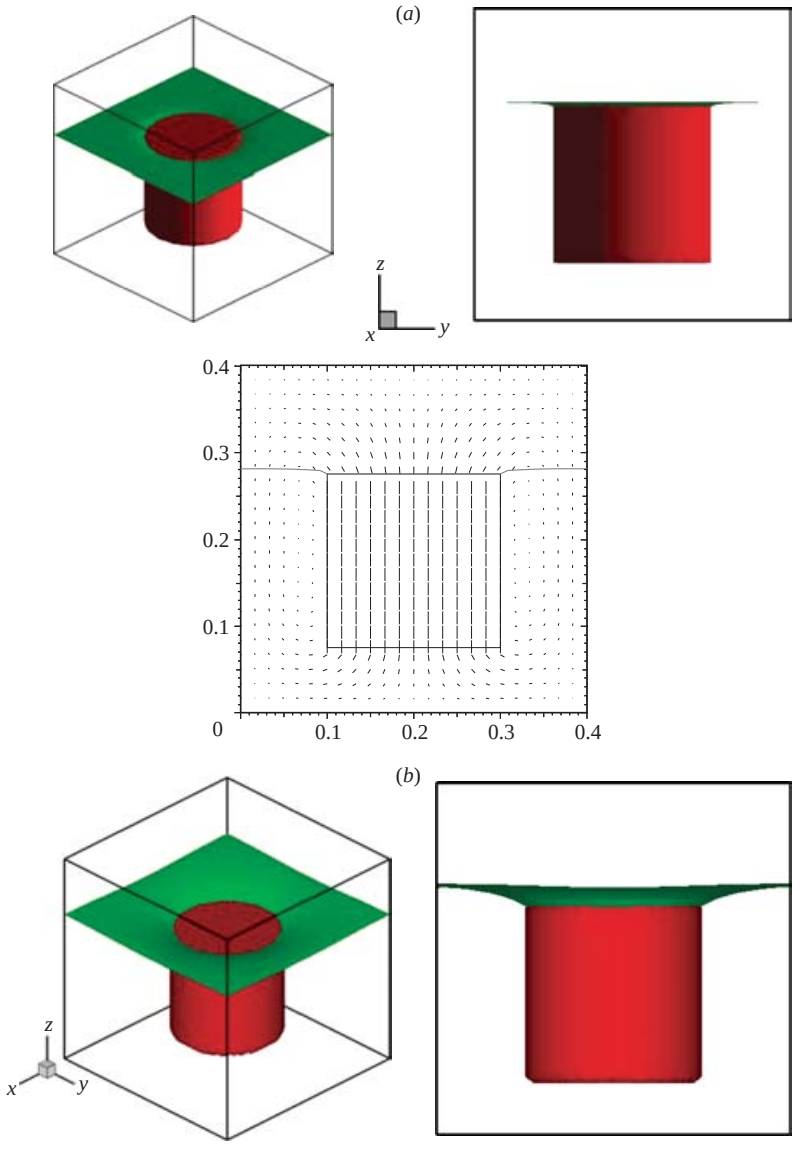

FIGURE 21. The disk position, the interface shape and the velocity field in the domain mid-section are shown. The length of velocity vectors is magnified 60 times and shown at every other node. The oblique and side views are shown. (*a*) $t = 0.0125$ s, (*b*) $t = 0.15$ s. The dimensionless parameters based on the maximum vertical velocity of the disk are ($Re = 0.35$, $G = 100.2$, $Ca = 0.014$) and based on the capillary velocity are ($Re = 50$, $G = 0.039$). After steady state is reached, the velocity is approximately zero everywhere in the domain.

greater depth and the contact angle is larger. In table 5 we give the computed values of h_2/R and the forces $F_p + F_c$ for the three values of ρ_p. For all cases, the computed values of the force are approximately equal to the weight of the disk. Some small differences are due to numerical errors. The equilibrium analysis of § 2 assumes that the fluid extends to infinity in the x-, y- and z-directions which is not the case for our simulations. This may explain small differences between our simulations and the analytical results.

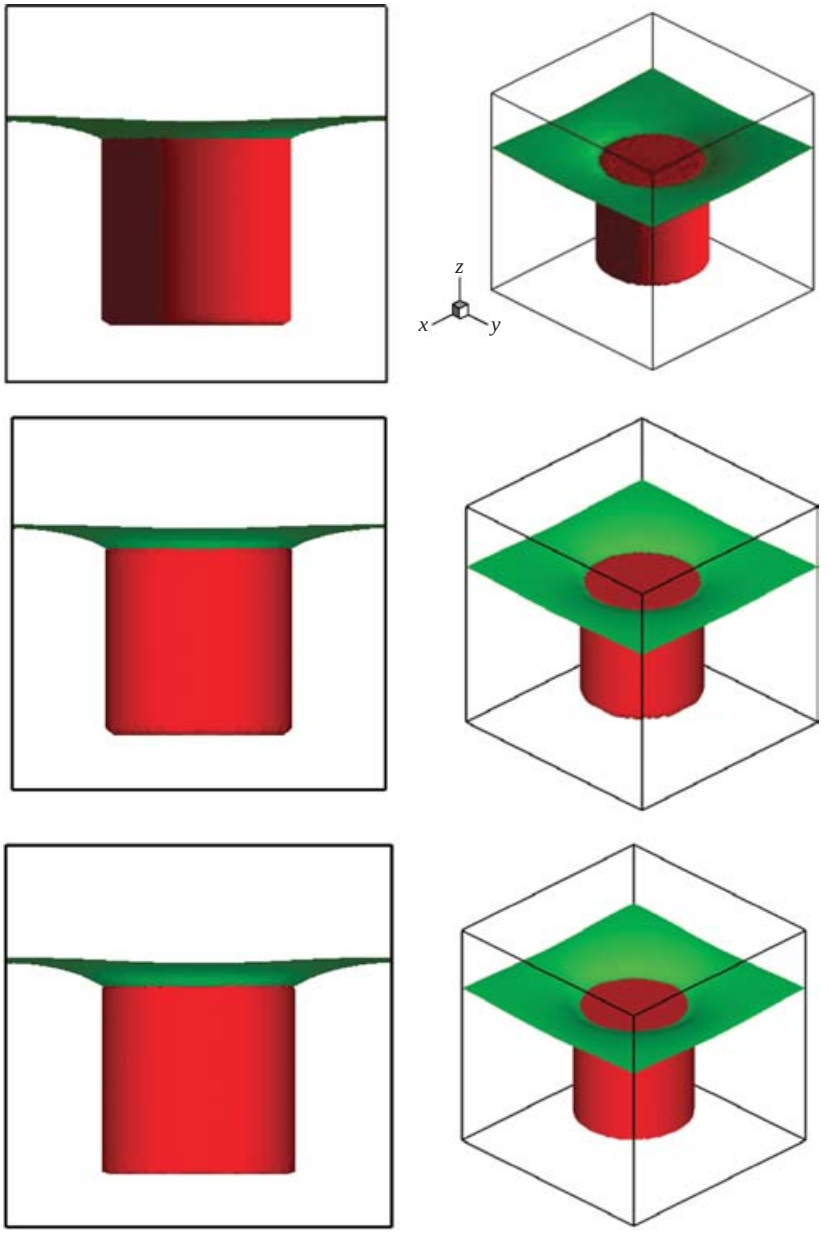

FIGURE 22. The oblique and front views of the floating disks and the interface shape. The depth to which a disk sinks into the lower fluid increases with increasing disk density. (*a*) $\rho_p = 1.1$, (*b*) $\rho_p = 1.2$, and (*c*) $\rho_p = 1.5$.

6.2.2. *Motion of two disks*

We next present results for the case where two disks are released near each other in the interface at the same vertical height. The domain height is 0.4 cm. The domain width along the x-direction is 0.8 cm and along the y-direction is 0.4 cm. The disk diameter is 0.1 cm and the height is 0.1 cm. The undeformed interface is at a distance

ρ (g cm^{-3})	weight (g cm s^{-2})	h_2/R	$F_p + F_c$ (g cm s^{-2})
1.1	6.78	0.15	6.86
1.2	7.40	0.21	7.38
1.5	9.24	0.28	9.26

TABLE 5. The interfacial deformation h_2/R and the sum of the pressure and vertical component of capillary forces obtained using (2.6) and (2.7) are shown as a function of the disk density. The interfacial tension is 5.0 dyn cm^{-1}. The density of lower fluid is 1.0 g cm^{-3} and that of the upper fluid is 0.1 g cm^{-3}. For all three cases, $F_p + F_c$ is approximately equal to the disk weight. Also notice that, as expected, the interface deformation increases with increasing particle density.

of 0.23 cm from the bottom. The initial velocities are assumed to be zero. The mesh resolution is comparable to that for the coarse mesh in § 6.2.1.

We first describe the case for which the particle density is 1.1 g cm^{-3}, the interfacial tension is 3.0 dyn cm^{-1}, and the upper fluid density and viscosity are 0.1 g cm^{-3} and 1.0 P, respectively. The viscosity of the lower fluid is 10.0 P. The two disks are placed at (0.32, 0.2, 0.18) and (0.48, 0.2, 0.18). The initial distance between the disks in the x-direction is $3.2R$. Figure 23(a) shows that at $t = 0.04$ the interface is deformed only in a small region around the disks and the disks do not experience a lateral attractive force. When the disks sink the contact angles increase. After this initial motion for $t \lesssim 0.12$ s, the disks sink slowly, as they move toward each other.

In figure 23(b) the disks and the interface shape are shown at $t = 0.2$ s. The interface height between the disks in figure 23(c) at $t = 0.5$ s is significantly lower than on the sides. Since the contact angle between the disks is smaller, the lateral capillary force is larger.

Figure 24(a) shows that the approach velocity $u_2 - u_1$ first increases and then decreases with time. The approach velocity increases with time because the lateral component of the capillary force increases as the distance between the disks decreases. This also causes the disks to slightly tilt in the (x, z)-plane. For all cases simulated in this paper it is smaller than 0.5°. The time taken by the disks to come together increases with the initial distance not only because the distance is larger, but also because the approach velocity decreases with increasing distance. Figure 24(a) also shows that the approach velocity starts to decrease when the gap between disks becomes small compared to the disk radius due to the activation of lubrication forces.

In figure 24 we have plotted the separation distance $d/R \geqslant 2$ and the approach velocity $u_2 - u_1$ as a function of time for three initial values of $d/R = (2.8, 3.2, 5.2)$ at $t = 0$. In all cases the approach velocity has a maximum value at a certain time and then decreases. The slow down is due to activation of lubrication force at close approach. The approach velocity in the case of the smallest initial distance $d/R = 2.8$ shown in figure 24(a) is negative for a short period and the particles first disperse and then attract.

The same type of plots are presented in figure 25 for the case in which the viscosity of the lower fluid is reduced tenfold, from 0.1 to 0.01 P and $d/R = 6$, larger even than $d/R = 5.2$ in figure 24(c). The magnitudes of the velocities which develop are larger in the small-viscosity fluid even though the initial separation is larger. The approach velocity is not monotonic due to changes in the interface shape away from the disk.

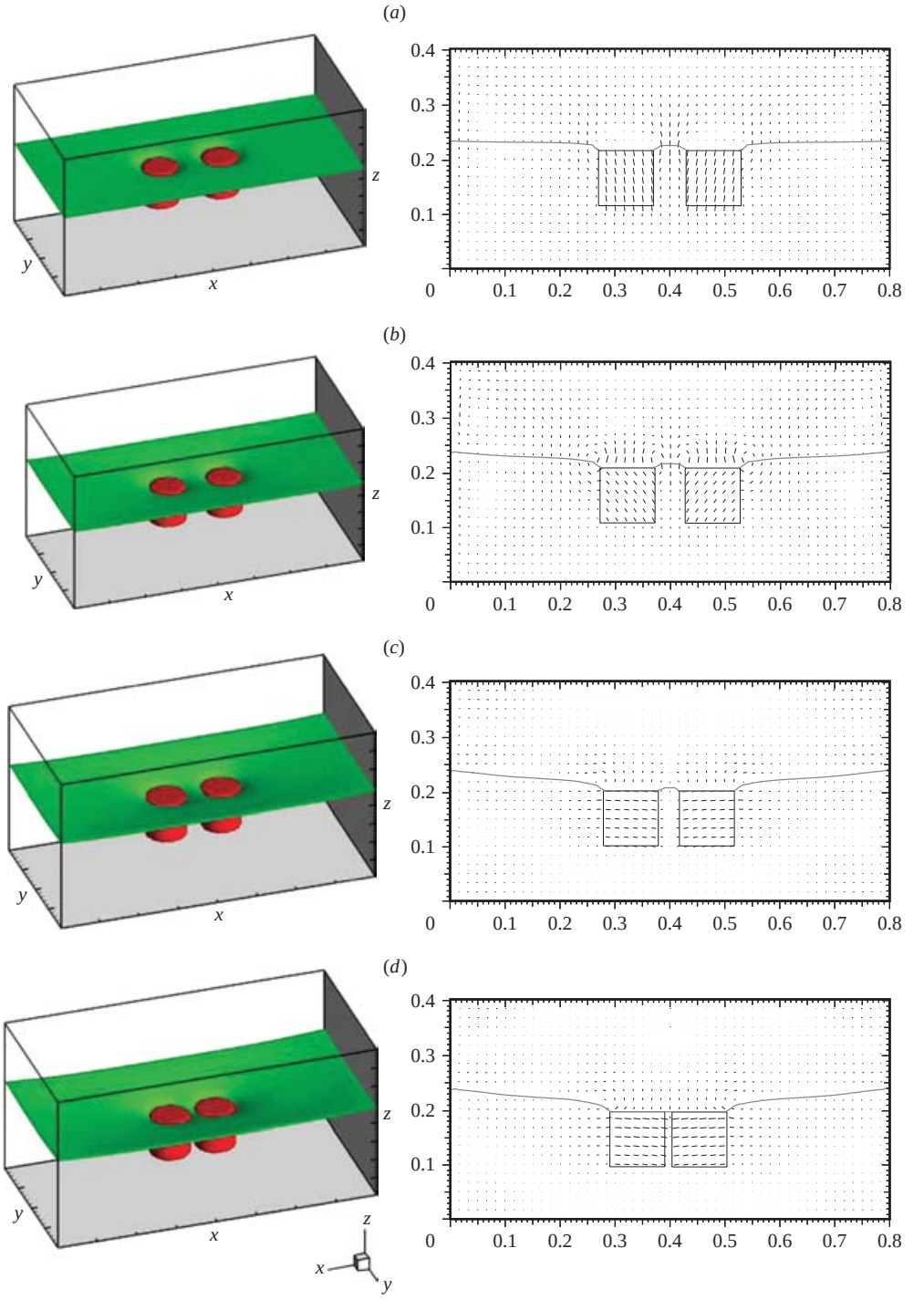

FIGURE 23. The positions of two disks suspended on the two-fluid interface and the velocity distribution at the domain midsection are shown at $t = 0.04$, 0.2, 0.5 and 0.8 s (*a–d*). The length of velocity vectors is magnified 100 times and shown at every other node. The disks move toward each other in the interface. The surface tension is 3.0 dyn cm^{-1}, the particle density is 1.1 g cm^{-3} and the density of the top fluid is 0.1 g cm^{-3} and that of the bottom fluid is 1.0 g cm^{-3}. The initial distance between the disks is $3.2R$. The dimensionless parameters based on the maximum velocity of the disk are ($Re = 0.0023$, $G = 242.0$, $Ca = 1.5$) and based on the capillary velocity are ($Re = 1.5 \times 10^{-3}$, $G = 545.0$).

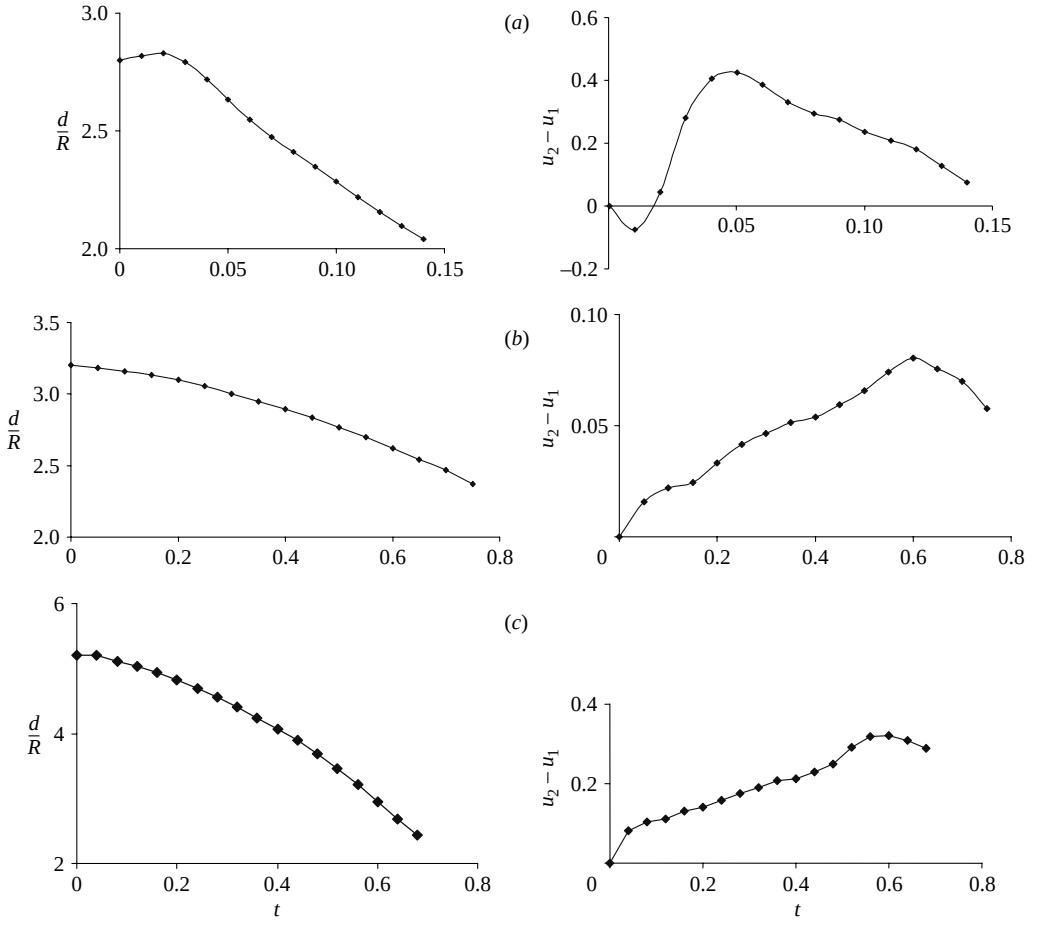

FIGURE 24. The approach velocity $u_2 - u_1$ and the dimensionless distance d/R between the disks are plotted as functions of time. The approach velocity initially increases as the interface height between the disks decreases and then decreases as the gap between the particles becomes small. (*a*) The initial distance between the disks is $2.8R$ and the dimensionless parameters based on the maximum disk velocity are ($Re = 0.11$, $G = 2224.5$, $Ca = 0.0021$). (*b*) The initial $d/R = 3.2$ and the dimensionless parameters are ($Re = 0.0023$, $G = 242.0$, $Ca = 1.5$). (*c*) The initial $d/R = 5.2$ and the dimensionless parameters are ($Re = 0.11$, $G = 2224.5$, $Ca = 0.0021$).

The tendency toward initial repulsion followed by attraction seen in figure 25 when the initial separation $d/R = 6$ is small has been observed in experiments. Joseph *et al.* (2003), state (p. 143)

> "We create such dispersions by pouring particles on the liquid, nothing complicated, just like a salt shaker. As soon as the particles hit the liquid surface they disperse radially leading to dispersions like that 3 minutes in figure 4. The dispersion, followed by attraction, is more or less universal and we have not seen it mentioned in the literature."

We expect the limiting value $d/R = 2$ to be achieved asymptotically as $t \to \infty$; this asymptotic result cannot be achieved with the present numerical package which uses a security zone to prevent collisions of particles. In the future we will implement the new scheme of Singh, Hesla & Joseph (2003) which does allow collision and close packing in equilibrium.

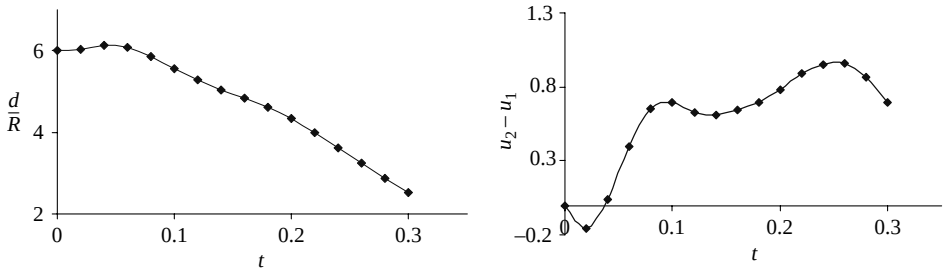

FIGURE 25. The approach velocity $u_2 - u_1$ and the dimensionless distance d/R between the disks are plotted as functions of time. The approach velocity initially increases as the interface height between the disks decreases and then decreases as the gap between the particles becomes small. The lower fluid viscosity is 0.01 P and the initial $d/R = 6$. The dimensionless parameters based on the maximum disk velocity are ($Re = 2.4$, $G = 425.8$, $Ca = 0.0024$).

ρ_p	ρ (upper fluid)	η (upper fluid)	γ	$(u_2 - u_1)_{max}$
1.1	1	0.1	10	0.0036
1.5	1	0.1	10	0.0762
1.5	0.1	0.01	10	0.034
2.0	0.1	0.01	10	0.066

TABLE 6. The maximum approach velocity for the disks is listed to show the dependence on their density. The lower fluid viscosity is 0.1 P and the density is 1.0 g cm^{-3}. The initial distance between the disks is $2.8R$.

Since the computational domain size for our simulations is only $8R$, the interface evolution near the particles is also influenced by the conditions imposed at the domain boundary. On the domain walls, the contact line does not remain flat; its level is lower in the middle of the domain walls and higher in the domain corners. This causes the particles' approach velocity to vary, as the lowering of contact lines on the domain walls influences the magnitude of the lateral attractive force, especially when the gap between the disk and a domain wall is comparable to the distance between the disks. This effect, which is due to a finite size of the computational domain, can be diminished by performing simulations in larger domains.

An interesting consequence of the lowering of the interface height between the disks is that the average value of the contact angle around the disk decreases. This decrease reduces the vertical component of capillary force which acts against gravity and keeps the disks floating. A reduction in the vertical capillary force causes the disks to sink slightly, increasing the contact angle everywhere except between the disks. After this additional sinking, the buoyant weight again becomes equal to the vertical component of the capillary force. This additional sinking, which also happens when two floating spheres come near each other, suggests that the clusters of disks are more likely to sink than an isolated disk.

Role of the particle density

In table 6 we have given results for the approach velocity for different values of the particle density. A denser disk sinks more causing a greater interfacial deformation. The lateral force which arises from the asymmetry is then greater and the velocity with which the disks approach each other is larger.

ρ_{lower}	ρ (upper fluid)	η (upper fluid)	γ	$(u_2 - u_1)_{max}$
1.0	1	0.1	10	0.0762
1.0	0.1	0.1	10	0.039

TABLE 7. The maximum approach velocities for the disks are listed to show dependence on the upper fluid density. The lower fluid viscosity is 0.1 Poise and the particle density is $1.5\,\mathrm{g\,cm^{-3}}$. The initial distance between the disks is $2.8R$.

ρ_{lower}	ρ (upper fluid)	η (upper fluid)	γ	$(u_2 - u_1)_{max}$
1.0	0.01	0.01	10	0.291
1.0	0.01	0.005	10	0.297

TABLE 8. The maximum approach velocities for the disks are listed to show the dependence on the upper fluid viscosity. The lower fluid viscosity is 0.1 P and the particle density is $2.0\,\mathrm{gm\,cm^{-3}}$. The initial distance between the disks is $2.8R$.

Role of the fluid density ratio

We now show how $u_2 - u_1$ depends on $l_U = \rho_U/\rho_L$. The case of matched densities $\rho_U = \rho_L$ is interesting because the lowering of the interface does not cause an increase in F_p. This case is also interesting because after the motion stops an equilibrium is reached in which the variation of pressure does not depend on the interface shape. This implies that the interface must deform so that there is no pressure jump across it; hence the mean curvature of the deformed interface is zero.

When the density ratio l_U is decreased the disks sink to a lower depth and their lateral approach velocities are smaller. The maximum approach velocities for two cases are listed in table 7.

Role of the viscosity ratio

We know that the viscosity does not play a role in determining the equilibrium state of floating particles, but it does alter the velocity. The lateral velocity of the disk decreases with increasing viscosity, but is not so strongly dependent on the viscosity ratio $m = \eta_U/\eta_L$.

In table 8 we have shown results for two different values of η_U/η_L. All other parameters are kept fixed. The approach velocity increases, but only slightly as the viscosity ratio is decreased. These velocities at a fixed distance of $2.7R$ are for the disks released at the initial distance of $2.8R$. The velocity increase is due to a decrease in the viscous resistance of the upper fluid. The increase in the velocity is greater for the heavier particles and also for larger values of l_U; in these cases the interfacial deformation is greater.

7. Conclusions

This paper is the first to be published on the direct numerical simulation of the motion of solid floating particles. A floating smooth particle, embedded in the interface between two fluids, touches the interface at a fixed contact angle, which at equilibrium is given by the Young–Dupré law. For a floating prismatic particle, on the other hand, the contact line is assumed to be fixed at its sharp edge, provided the contact angle at the edge is within the limits specified by the Gibbs extension to the Young–Dupré law. For example, in our simulations of disks, floating with their axis normal to the interface, the contact line is assumed to be pinned at the top sharp edge of the disk.

The constraint that the contact line remains pinned at a sharp edge of a prismatic particle is different from that for a smooth particle, such as a sphere. For a smooth particle, the contact line can move, but the contact angle is fixed and here is assumed to be that at equilibrium given by the Young–Dupré law. The problem of the motion of the contact line is difficult and unsolved. The difficulty is that the no-slip condition implies that the contact point cannot move which contradicts the behaviour seen in experiments (see Dussan V. & Davis 1974; Dussan V. 1976; Kistler & Scriven 1993 and references therein). Several approaches to this problem have been proposed and could be implemented in direct numerical simulations (see Sussman 2001; Friedrichs & Guceri 1993; Kamal *et al.* 1988, and references therein). Here we look at one approach which could be called capillary-induced motion of the contact line due to a prescribed contact angle. In this approach, we let the contact line adjust to the dynamics under the constraint that the contact angle is fixed. The no-slip condition is satisfied before and after the contact line moves. In another approach, not implemented here, the contact line is allowed to slip by relaxing the no-slip condition by making the velocity of the contact line proportional to the shear stress there. This approach requires us to relax the prescribed contact angle condition. Another feature, not treated here, which has an impact on the floating particle problem is the existence of advancing and receding contact angles. The subject is very rich with many possibilities that might be studied in direct simulations.

The Marchuk–Yenenko operator-splitting technique is used to decouple the four primary numerical difficulties of the governing equations: incompressibility constraint, nonlinear convection term, Lagrange multiplier problem that forces rigid-body motion within the particles, and the interface advection problem. The resulting four sub-problems are solved efficiently using matrix-free approaches. Specifically, the DLM approach is used for enforcing rigid-body motion inside the particles, the level-set approach for tracking the interface and the conjugate gradient algorithms are used to enforce the incompressibility constraint and to solve the nonlinear convection problem. The contact line is kept at a sharp edge by making the level-set function zero along the edge. On smooth surfaces the contact angle is kept fixed by using the technique described above. The code is validated by simulating the time-dependent motion of a particle released on a two-fluid interface to steady state.

Our simulations show that the interface shape near a sphere adjusts quickly after it is released to meet the contact angle requirement, but away from the sphere the interface shape takes a much longer time interval to adjust during which the vertical position of the particle changes. The computed results are shown to be independent of the mesh resolution as well as of the size of time step. The steady-state limits of our dynamic simulations agree with the equilibrium results. The time-dependent simulations of two or more floating particles lead to capillary attraction and the formation of clusters. The attractive capillary force arises due to the asymmetric interface deformation around the particles. Specifically, the interface height between the particles is lowered giving rise to a lateral attractive force due to capillarity. This lowering of the interface also decreases the net vertical component of the capillary force which causes the floating height of the particles to decrease. These results agree qualitatively with the experimental data as well as the equilibrium analysis.

For floating disks, simulations are started by assuming that the interface is flat and that the top surface of the disk is in the plane of the interface, ensuring that the contact line is initially pinned at the sharp rim. The disk assumed to be denser than the liquid sinks into the lower liquid. As it sinks, the contact angle increases which in turn increases the vertical component of the capillary force. The disk stops

sinking when its buoyant weight is balanced by the capillary force. The code is validated by simulating the time-dependent motion of a disk released on a two-fluid interface to steady state. Simulations show that as the disk sinks, the interface near the disk moves downward, as the contact line is pinned to the edge, but away from the disk the interface shape takes a longer time interval to adjust during which the vertical position of the disk changes. The computed results are independent of the mesh resolution as well as of the size of the time step. The steady-state limits of our dynamic simulations agree with the equilibrium results.

Simulations also show that the lowering of the interface between disks pinned to the interface at the rim reduces the contact angle between the disks giving rise to an unbalanced attractive capillary force. Two floating spheres also attract, but the mechanism by which the attractive force arises is different. Specifically, the lateral force on two floating spheres arises due to the lowering of the contact line on the surfaces between the two spheres which is a consequence of the constraint that the contact angle is fixed. For floating disks, on the other hand, the contact line is fixed and the lateral force arises due to a decrease in the contact angle between the disks due to the lowering of the interface. The lowering of the interface also decreases the net vertical component of the capillary force which causes the floating height of the particles to decrease.

Though our floating particle code has been optimized in various ways it still runs slowly. Improvements can be made by parallelizing the code for machines with large clusters. The security zone which has been used in previous direct numerical simulation based studies, and this one, does not allow contact between particles and hence is not faithful to the crystal structures which can evolve in problems of self-assembly due to capillary attraction. Fortunately, the new collision scheme put forward by Singh *et al.* (2003) does allow particle–particle contact and close packing. We will implement this new strategy in our future work.

This paper is dedicated to Professor Stan Osher on the occasion of his 60th birthday. This work was partially supported by National Science Foundation KDI Grand Challenge grant (NSF/CTS-98-73236) and a GOALI grant NSF/CTS-0109079, Engineering Research Program of the Office of Basic Energy Science at DOE, a grant from Schlumberger foundation, from STIM-LAB Inc., New Jersey Commission on Science and Technology through the New-Jersey Centre for Micro-Flow Control under (Award Number 01-2042-007-25) and the University of Minnesota Supercomputing Institute.

Appendix. Weak form of equations and finite-element discretization

The approach used for obtaining the weak form of the governing equations for the fluid–particle systems was described in Glowinski *et al.* (1999) and Singh *et al.* (2000). In obtaining this weak form, the hydrodynamic forces and torques acting on the particles can be completely eliminated by combining the fluid and particle equations of motion into a single weak equation of motion for the combined fluid–particle system. The hydrodynamic stresses acting at the interface are also completely eliminated. For simplicity, in this section we will assume that there is only one particle. The extension to the many-particle case is straightforward.

The solution and variation are required to satisfy the strong form of the constraint of rigid-body motion throughout $P(t)$. In the distributed Lagrange multiplier method this constraint is removed from the velocity space and enforced weakly as a side constraint

using a distributed Lagrange multiplier term. The following weak formulation of the problem holds in the extended domain:

For a.e. $t > 0$, find $\boldsymbol{u} \in \overline{W}_{u\Gamma}$, $p \in L^2_0(\Omega)$, $\boldsymbol{\lambda} \in \Lambda(t)$, $\boldsymbol{U} \in \boldsymbol{R}^3$, $\boldsymbol{\omega} \in \boldsymbol{R}^3$ and $\phi \in W_\phi$, satisfying

$$\begin{aligned}
&\int_\Omega \rho\left(\frac{\mathrm{d}\boldsymbol{u}}{\mathrm{d}t} - \boldsymbol{g}\right)\cdot\boldsymbol{v}\,\mathrm{d}\boldsymbol{x} - \int_\Omega p\nabla\cdot\boldsymbol{v}\,\mathrm{d}\boldsymbol{x} + \int_\Omega 2\eta\boldsymbol{D}[\boldsymbol{u}]:\boldsymbol{D}[\boldsymbol{v}]\,\mathrm{d}\boldsymbol{x} \\
&\quad + \left(1 - \frac{\rho}{\rho_d}\right)\left(M\left(\frac{\mathrm{d}\boldsymbol{U}}{\mathrm{d}t} - \boldsymbol{g}\right)\cdot\boldsymbol{V} + I\frac{\mathrm{d}\boldsymbol{\omega}}{\mathrm{d}t}\boldsymbol{\xi}\right) - \boldsymbol{F}'\cdot\boldsymbol{V} - \int_\Omega \gamma\kappa\delta(\phi)\,\boldsymbol{n}\cdot\boldsymbol{v}\,\mathrm{d}\boldsymbol{x} \\
&\quad = \langle\boldsymbol{\lambda}, \boldsymbol{v} - (\boldsymbol{V} + \boldsymbol{\xi}\times\boldsymbol{r})\rangle_{P(t)} \quad \text{for all} \quad \boldsymbol{v} \in \overline{W}_0,\ \boldsymbol{V} \in \boldsymbol{R}^3, \text{and } \boldsymbol{\xi} \in \boldsymbol{R}^3, \qquad \text{(A 1)}
\end{aligned}$$

$$\int_\Omega q\nabla\cdot\boldsymbol{u}\,\mathrm{d}\boldsymbol{x} = 0 \quad \text{for all } q \in L^2(\Omega), \qquad \text{(A 2)}$$

$$\langle\boldsymbol{\mu}, \boldsymbol{u} - (\boldsymbol{U} + \omega\times\boldsymbol{r})\rangle_{P(t)} = 0 \quad \text{for all } \boldsymbol{\mu} \in \boldsymbol{\Lambda}(t), \qquad \text{(A 3)}$$

$$\boldsymbol{u}|_{t=0} = \boldsymbol{u}_o \quad \text{in } \Omega, \qquad \text{(A 4)}$$

$$\int_\Omega \left(\frac{\partial\phi}{\partial t} + \boldsymbol{u}\cdot\nabla\phi\right)g\,\mathrm{d}\boldsymbol{x} = 0 \quad \text{for all } g \in W_{\phi 0}, \qquad \text{(A 5)}$$

$$\phi|_{t=0} = \phi_0 \quad \text{in } \Omega,$$

as well as the kinematic equations and the initial conditions for the particle linear and angular velocities. Here $\boldsymbol{F}'$ is the additional body force applied to the particles to limit the extent of overlap (see equation (19) in Glowinski *et al.* 1999), $\boldsymbol{\lambda}$ is the distributed Lagrange multiplier,

$$\left.\begin{aligned}
&\overline{W}_{u\Gamma} = \{\boldsymbol{v} \in H^1(\Omega)^3 | \boldsymbol{v} = \boldsymbol{u}_\Gamma(t) \quad \text{on} \quad \Gamma\},\\
&\overline{W}_0 = H^1_0(\Omega)^3,\\
&L^2_0(\Omega) = \{q \in L^2(\Omega) | \textstyle\int_\Omega q\,\mathrm{d}\boldsymbol{x} = 0\},\\
&W_\phi = \{\phi \in H^1(\Omega) | \phi = \phi_0(t) \quad \text{on} \quad \Gamma^-\},\\
&W_{\phi 0} = \{\phi \in H^1(\Omega) | \phi = 0 \quad \text{on} \quad \Gamma^-\},
\end{aligned}\right\} \qquad \text{(A 6)}$$

where Γ^- is the upstream part of Γ and $\Lambda(t)$ is $L^2(P(t))^3$, with $\langle .,. \rangle_{P(t)}$ denoting the L^2 inner product over the particle. In our simulations, since the velocity and $\boldsymbol{\mu}$ are in L^2, we will use the following inner product:

$$\langle\boldsymbol{\mu}, \boldsymbol{v}\rangle_{P(t)} = \int_{P(t)} (\boldsymbol{\mu}\cdot\boldsymbol{v})\,\mathrm{d}\boldsymbol{x}. \qquad \text{(A 7)}$$

In order to solve the above problem numerically, we will discretize the domain using a regular tetrahedral mesh T_h for the velocity, where h is the mesh size, and a regular tetrahedral mesh T_{2h} for the pressure. The following finite dimensional spaces are defined for approximating $\overline{W}_{u\Gamma}$, $\overline{W}_0$, $L^2(\Omega)$, $L^2_0(\Omega)$, W_ϕ and $W_{\phi 0}$:

$$\left.\begin{aligned}
&W_{u\Gamma,h} = \{\boldsymbol{v}_h \in C^0(\overline{\Omega})^3 | \boldsymbol{v}_h|_T \in P_1\times P_1\times P_1 \quad \text{for all } T \in T_h,\ \boldsymbol{v}_h = \boldsymbol{u}_{\Gamma,h} \text{ on } \Gamma\},\\
&W_{0,h} = \{\boldsymbol{v}_h \in C^0(\overline{\Omega})^3 | \boldsymbol{v}_h|_T \in P_1\times P_1\times P_1 \quad \text{for all } T \in T_h,\ \boldsymbol{v}_h = 0 \text{ on } \Gamma\},\\
&L^2_h = \{q_h \in C^0(\overline{\Omega}) | q_h|_T \in P_1 \quad \text{for all } T \in T_{2h}\},\\
&L^2_{0,h} = \{q_h \in L^2_h | \textstyle\int_\Omega q_h\,\mathrm{d}\boldsymbol{x} = 0\},\\
&W_{\phi,h} = \{g_h \in H^1(\Omega) | g_h|_T \in P_1 \quad \text{for all } T \in T_h,\ g_h = \phi^n \text{ on } \Gamma^-\}\\
&W_{\phi 0,h} = \{g_h \in H^1(\Omega) | g_h|_T \in P_1 \quad \text{for all } T \in T_h,\ g_h = 0 \text{ on } \Gamma^-\}\\
&W_{\phi R,h} = \{g_h \in H^1(\Omega) | g_h|_T \in P_1 \quad \text{for all } T \in T_h,\ g_h = 0 \text{ on the interface}\}.
\end{aligned}\right\} \qquad \text{(A 8)}$$

The particle inner product terms in (A 1) and (A 3) are obtained using the discrete L^2 inner product defined in Glowinski *et al.* (1999). Specifically, we choose M points, $\boldsymbol{x}_1, \ldots, \boldsymbol{x}_M$ that uniformly cover $\overline{P}(t)$, and define

$$\boldsymbol{\Lambda}_h(t) = \left\{ \boldsymbol{\mu}_h | \boldsymbol{\mu} = \sum_{i=1}^{M} \boldsymbol{\mu}_{h,i} \delta(\boldsymbol{x} - \boldsymbol{x}_i), \quad \boldsymbol{\mu}_{h,1}, \ldots, \boldsymbol{\mu}_{h,M} \in \boldsymbol{R}^3 \right\}.$$

Using these finite dimensional spaces, it is straightforward to discretize equations (A 1) – (A 5). Notice that the discrete space $W_{\phi,h}$ assumes that ϕ is known on the upstream portion of the boundary. This is not a problem even when $\phi(t)$ is not known on the upstream boundary in advance because the imposed boundary value can be corrected during the reinitialization step. Since only the zero level set of $\phi(t)$ is physically relevant, we have a lot of freedom in treating $\phi(t)$ away from the interface. In our code, the value from the previous time step is used as the boundary value. The reinitialization space $W_{\phi R,h}$ assumes that ϕ remains zero along the interface which is done by imposing the Dirichlet boundary condition, $\phi = 0$, along the interface during reinitialization iterations.

A.1. *Strong form*

The strong form for the weak formulation can be obtained by integrating the stress term by parts. The resulting equations inside the region occupied by the fluid $\Omega \backslash \overline{P(t)}$ are

$$\rho \left[\frac{\partial \boldsymbol{u}}{\partial t} + \boldsymbol{u} \cdot \nabla \boldsymbol{u} \right] = \rho \boldsymbol{g} - \nabla p + \nabla \cdot \boldsymbol{\sigma} + \gamma \kappa \delta(\phi) \boldsymbol{n} \quad \text{in } \Omega \backslash \overline{\mathrm{P(t)}},$$

$$\nabla \cdot \boldsymbol{u} = 0 \quad \text{in } \Omega \backslash \overline{\mathrm{P(t)}},$$

$$\boldsymbol{u} = \boldsymbol{u}_L \quad \text{on } \Gamma_d,$$

$$\boldsymbol{u} = \boldsymbol{U} + \omega \times \boldsymbol{r} \quad \text{on } \partial P(t),$$

and the equations inside the region occupied by the particles $P(t)$ are

$$\rho \left[\frac{\partial \boldsymbol{u}}{\partial t} + \boldsymbol{u} \cdot \nabla \boldsymbol{u} \right] = \rho \boldsymbol{g} - \nabla p + \nabla \cdot (2\eta \boldsymbol{D}) + \boldsymbol{\lambda} - R^2 \nabla^2 \boldsymbol{\lambda}, \tag{A 9}$$

$$\boldsymbol{u} = \boldsymbol{U}_i + \omega_i \times \boldsymbol{r}_i \quad \text{on} \quad \partial P_i(t), i = 1, \ldots, N.$$

Here we have used the fact that the rigid-body motion satisfies the incompressibility constraint and that $\boldsymbol{D}(\boldsymbol{u})$ inside the particles is zero. The boundary condition for $\boldsymbol{\lambda}$ on the interface between the fluid and particle regions $\partial P(t)$ is

$$\boldsymbol{n} \cdot (-\sigma_L) = \boldsymbol{n} \cdot \nabla \boldsymbol{\lambda} \tag{A 10}$$

where $\boldsymbol{n}$ is the normal at the fluid–particle interface, and $\sigma_L = -p\boldsymbol{I} + 2\eta \boldsymbol{D}$ is the stress in the fluid phase, and $\sigma_P = 0$ is the stress inside the particles. For given $\boldsymbol{U}(t)$ and $\omega(t)$, and the positions $X_i(t), i = 1, \ldots, N$, equation (A 9) can be written as

$$\boldsymbol{\lambda} - R^2 \nabla^2 \boldsymbol{\lambda} = \rho_L \left(\frac{\mathrm{d}\boldsymbol{U}}{\mathrm{d}t} + \frac{\mathrm{d}\omega}{\mathrm{d}t} \times \boldsymbol{r} + \omega \times (\omega \times \boldsymbol{r}) \; - \boldsymbol{g} \right) \tag{A 11}$$

It is shown in Joseph (2002, chapter IV), that it is possible to completely eliminate the Lagrange multiplier λ from the strong form.

A.2. *Time discretization using the Marchuk–Yanenko operator splitting scheme*

The discretized initial value problem (A 1–A 5) is solved by using the Marchuk–Yanenko operator splitting scheme. This allows us to decouple its four primary

difficulties:

1. the incompressibility condition and the related unknown pressure p_h,
2. the nonlinear convection term,
3. the rigid body motion problem inside the particles,
4. the interface problem and the related unknown level set distribution ϕ_h.

The Marchuk–Yanenko operator splitting scheme can be applied to an initial value problem of the form

$$\frac{\mathrm{d}\phi}{\mathrm{d}t} + A_1(\phi) + A_2(\phi) + A_3(\phi) + A_4(\phi) = f$$

where the operators A_1, A_2, A_3, and A_4 can be multiple-valued.

Let Δt be the time step, and α_1 and α_2 be two constants: $0 \leqslant \alpha_1$, $\alpha_2 \leqslant 1$ and $\alpha_1 + \alpha_2 = 1$. We use the following version of the Marchuk–Yanenko operator splitting to simulate the motion of particles on two-fluid interfaces:

Set $\boldsymbol{u}^0 = \boldsymbol{u}_{0,h}$, and $\phi^0 = \phi_{0,h}$.

For $n = 0, 1, 2, \ldots$ assuming $\boldsymbol{u}^n$, and ϕ^n are known, find the values for $n+1$ using the following:

Step 1:

Find $\boldsymbol{u}^{n+1/4} \in W_{u,h}$ and $p^{n+1/4} \in L^2_{0,h}$, by solving

$$\left.\begin{aligned} &\int_\Omega \rho \frac{\boldsymbol{u}^{n+1/4} - \boldsymbol{u}^n}{\Delta t} \cdot \boldsymbol{v}\, \mathrm{d}\boldsymbol{x} - \int_\Omega p^{n+1/4} \nabla \cdot \boldsymbol{v}\, \mathrm{d}\boldsymbol{x} \\ &\quad = \int_\Omega \gamma \kappa \delta(\phi)\, \boldsymbol{n} \cdot \boldsymbol{v}\, \mathrm{d}\boldsymbol{x} \quad \text{for all } \boldsymbol{v} \in W_{0,h}, \\ &\int_\Omega q \nabla \cdot \boldsymbol{u}^{n+1/4}\, \mathrm{d}x = 0 \quad \text{for all } q \in L^2_h. \end{aligned}\right\} \tag{A 12}$$

Step 2:

Find $\boldsymbol{u}^{n+2/4} \in W_{u,h}$, by solving

$$\int_\Omega \rho \frac{\boldsymbol{u}^{n+2/4} - \boldsymbol{u}^{n+1/4}}{\Delta t} \cdot \boldsymbol{v}\, \mathrm{d}\boldsymbol{x} + \int_\Omega \rho \left(\boldsymbol{u}^{n+2/4} \cdot \nabla \boldsymbol{u}^{n+2/4}\right) \cdot \boldsymbol{v}\, \mathrm{d}\boldsymbol{x} + \alpha_1 \int_\Omega 2\eta \boldsymbol{D}\left[\boldsymbol{u}^{n+2/4}\right] : \boldsymbol{D}[\boldsymbol{v}]\, \mathrm{d}\boldsymbol{x} = 0 \quad \text{for all } \boldsymbol{v} \in W_{0,h}. \tag{A 13}$$

Step 3:

Compute $\boldsymbol{U}^{n+3/4}$ and $\boldsymbol{X}^{n+3/4}$ using the prediction procedure

Set $\boldsymbol{U}^{n,0} = \boldsymbol{U}^n$, $\boldsymbol{X}^{n,0} = \boldsymbol{X}^n$.

Do $k = 1, K$

$$\boldsymbol{U}^{*n,k} = \boldsymbol{U}^{n,k-1} + \left(\boldsymbol{g} + \left(1 - \frac{\rho}{\rho_d}\right)^{-1} M^{-1} F'(X^{n,k-1})\right) \frac{\Delta t}{K}$$

$$\boldsymbol{X}^{*n,k} = \boldsymbol{X}^{n,k-1} + \left(\frac{\boldsymbol{U}^{n,k-1} + \boldsymbol{U}^{*n,k}}{2}\right) \frac{\Delta t}{K},$$

$$\boldsymbol{U}^{n,k} = \boldsymbol{U}^{n,k-1} + \left(\boldsymbol{g} + \left(1 - \frac{\rho}{\rho_d}\right)^{-1} M^{-1} \frac{F'(X^{n,k-1}) + F'(X^{*n,k-1})}{2}\right)\frac{\Delta t}{K},$$

$$\boldsymbol{X}^{n,k} = \boldsymbol{X}^{n,k-1} + \left(\frac{\boldsymbol{U}^{n,k-1} + \boldsymbol{U}^{n,k}}{2}\right)\frac{\Delta t}{K},$$

end do

Set $\boldsymbol{U}^{n+3/4} = \boldsymbol{U}^{n,K}$, $\boldsymbol{X}^{n+3/4} = \boldsymbol{X}^{n,K}$. (A 14)

Find $\boldsymbol{u}^{n+1} \in W^{n+1}_{u\Gamma,h}$, $\boldsymbol{\lambda}^{n+1} \in \Lambda_h((n+2/4)\Delta t)$, $\boldsymbol{U}^{n+1} \in \boldsymbol{R}^3$, and $\boldsymbol{\omega}^{n+1} \in \boldsymbol{R}^3$, satisfying

$$\int_\Omega \rho \frac{\boldsymbol{u}^{n+1} - \boldsymbol{u}^{n+2/4}}{\Delta t} \cdot \boldsymbol{v}\, \mathrm{d}\boldsymbol{x} + \left(1 - \frac{\rho}{\rho_d}\right)\left(M \frac{\boldsymbol{U}^{n+1} - \boldsymbol{U}^{n+3/4}}{\Delta t} \cdot \boldsymbol{V} + I \frac{\boldsymbol{\omega}^{n+1} - \boldsymbol{\omega}^{n+3/4}}{\Delta t} \boldsymbol{\xi}\right)$$
$$+ \gamma \int_\Omega 2\eta \boldsymbol{D}[\boldsymbol{u}^{n+1}] : \boldsymbol{D}[\boldsymbol{v}]\, \mathrm{d}\boldsymbol{x}$$
$$= \left\langle \boldsymbol{\lambda}^{n+1}, \boldsymbol{v} - \left(\boldsymbol{V} + \boldsymbol{\xi} \times \boldsymbol{r}^{n+3/4}\right)\right\rangle_{P((n+3/4)\Delta t)} \quad \text{for all } \boldsymbol{v} \in W_{0,h},\ \boldsymbol{V} \in \boldsymbol{R}^3, \quad \text{and } \boldsymbol{\xi} \in R^3$$

$$\langle \boldsymbol{\mu}_h, \boldsymbol{u}^{n+1} - (\boldsymbol{U}^{n+1} + \boldsymbol{\omega}^{n+1} \times \boldsymbol{r})\rangle_{P((n+3/4)\Delta t)} = 0 \quad \text{for all} \quad \boldsymbol{\mu}_h \in \boldsymbol{\Lambda}((n+3/4)\Delta t), \quad \text{(A 15)}$$

where the centre of particle $P((n+3/4)\Delta t)$ is at $\boldsymbol{X}^{n+3/4}$. For a disk the moment of inertia changes as the disk rotates and so we also keep track of its orientation.

Set $\boldsymbol{X}^{n+1,0} = \boldsymbol{X}^n$.

Do $k = 1, K$

$$\boldsymbol{X}^{*n+1,k} = \boldsymbol{X}^{n+1,k-1} + \left(\frac{\boldsymbol{U}^n + \boldsymbol{U}^{n+1}}{2}\right)\frac{\Delta t}{K},$$

$$\boldsymbol{X}^{n,k} = \boldsymbol{X}^{*n,k-1} + \left(1 - \frac{\rho}{\rho_d}\right)^{-1} M^{-1}\left(\frac{F'(X^{n+1,k-1}) + F'(X^{*n+1,k})}{2}\right)\frac{(\Delta t)^2}{2K},$$

end do

Set $\boldsymbol{X}^{n+1} = \boldsymbol{X}^{n+1,K}$.

Step 4:

Find $\phi^{n+4/4} \in W^n_{\phi,h}$, by solving

$$\int_\Omega \left(\frac{\phi^{n+4/4} - \phi^n}{\Delta t} + \boldsymbol{u}^{n+1} \cdot \nabla \phi^{n+1}\right) g_h\, \mathrm{d}\boldsymbol{x} = 0 \quad \text{for all } g_h \in W_{\phi 0,h}. \quad \text{(A 16)}$$

Set $p^{n+1} = p^{n+1/4}$, $\phi^{n+1} = \phi^{n+4/4}$.

Step 4.1:

Reinitialize ϕ^{n+1}

Set $\phi^0_R = \phi^{n+1}$

For $r = 0, 1, 2, \ldots$

$$w^r = S(\phi^{n+1}) \frac{\nabla \phi^r_R}{|\nabla \phi^r_R|}$$

Find $\phi^{r+1}_R \in W_{\phi R,h}$, by solving

$$\int_\Omega \left(\frac{\phi^{r+1}_R - \phi^r_R}{\Delta t} + \boldsymbol{w}^r \cdot \nabla \phi^r_R\right) g_h\, \mathrm{d}\boldsymbol{x} = \int_\Omega S(\phi^{n+1}) g_h\, \mathrm{d}x \quad \text{for all } g_h \in W_{\phi R,h}. \quad \text{(A 17)}$$

Go back to the above for loop.

Step 4.2:

Modify ϕ^{n+1} inside and on the particle surfaces to enforce contact angle

Set $\phi_R^0 = \phi^{n+1}$

For $r = 0, 1, 2, \ldots$

$$\boldsymbol{u}_{ex}^r = \begin{cases} 0 & \text{outside particles} \\ \boldsymbol{u}_{ex} \text{ from (5.6)} & \text{otherwise.} \end{cases}$$

Find $\phi_R^{r+1} \in W_{\phi R,h}$, by solving

$$\int_\Omega \left(\frac{\phi_R^{r+1} - \phi_R^r}{\Delta t} + \boldsymbol{u}_{ex}^r \cdot \nabla \phi_R^r \right) g_h \, \mathrm{d}x = 0 \quad \text{for all } g_h \in W_{\phi R,h}. \tag{A 18}$$

Go back to the above for loop.

Set $\phi^{n+1} = \phi_R^{r+1}$ and go back to the first step.

The decoupled sub-problems can be solved much more efficiently than the original problem (A 1–A 5). In our code all of these sub-problems are solved using matrix-free algorithms, which reduces the memory required.

Remarks:

1. The first step gives rise to a L^2 projection problem for the velocity and pressure distributions which is solved by using a conjugate gradient method (Glowinski *et al.* 1992, 1999).

2. The second step is a nonlinear problem for the velocity, which is solved by using a least square conjugate gradient algorithm (Glowinski & Pironneau 1992).

3. In this paper, we will assume that $\alpha_1 = 1$, $\alpha_2 = 0$.

4. The fourth step is a hyperbolic problem for the scalar level-set function ϕ. This problem is solved by using an upwinding scheme where the advection term is discretized using a third-order scheme (Glowinski & Pironneau 1992 and Pillapakkam & Singh 2001).

5. After advecting ϕ according to (A 16), we reinitialize ϕ to be a distance function near the interface by performing one or two iterations of (A 17) using a fast algorithm developed in Pillaipakkam & Singh (2001). The interface position $\phi(t) = 0$ does not change during these reinitialization iterations. It is necessary to re-initialize ϕ to ensure that the scheme accurately conserves mass.

6. The level-set function is extended inside and on the surface of the particles such that the contact angle is 135° by performing one or two iterations of (A 18).

REFERENCES

Bowden, N., Choi, I. S., Grzybowski, B. A. & Whitesides, G. M. 1999 Mesoscale self-assembly of hexagonal plates using lateral capillary forces: synthesis using the "capillary bond". *J. Am. Chem. Soc.* **121**, 5373.

Bowden, N., Terfort, A., Carbeck, J. & Whitesides, G. M. 1997 Self-assembly of mesoscale objects into ordered two-dimensional arrays. *Science* **276**, 233.

Brenner, H. & Leal, L. G. 1978 A micromechanical derivation of Fick's law for interfacial diffusion of surfactant molecules. *J. Colloid Interface Sci.* **65**, 191.

Brenner, H. & Leal, L. G. 1982 Conservation and constitutive equations for adsorbed species undergoing surface diffusion and convection at a fluid-fluid interface. *J. Colloid Interface Sci.* **88**, 136.

Bristeau, M. O., Glowinski, R. & Periaux, J. 1987 Numerical methods for Navier-Stokes equations. Application to the simulation of compressible and incompressible flows. *Computer Phys. Rep.* **6**, 73.

Chan, D. Y. C., Henry Jr., J. D. & White, L. R. 1981 The interaction of colloidal particles collected at the fluid interface. *J. Colloid Interface Sci.* **79**, 410.

Danov, K. D., Aust, R., Durst, F. & Lange, U. 1995 Influence of the surface viscosity on the hydrodynamic resistance and surface diffusivity of a large Brownian particle. *J. Colloid Interface Sci.* **175**, 36–45.

Dussan, V. E. B. 1976 The moving contact line: the slip boundary condition. *J. Fluid Mech.* **77**, 665–684.

Dussan, V. E. B. & Davis, S. H. 1974 On the motion of a fluid-fluid interface along a solid surface. *J. Fluid Mech.* **65**, 71.

Fortes, M. A. 1982 Attraction and repulsion of floating particles. *Can. J. Chem.* **60**, 2889.

Friedrichs, B. & Guceri, S. I. 1993 A novel hybrid numerical technique to model 3-D fountain flow in injection molding processes. *J. Non-Newtonian Fluid Mech.* **49**, 141–173.

Gerson, D. F., Zaijc, J. E. & Ouchi, M. D. 1979 In *Chemistry for Energy* (ed. M. Tomlinson). ACS symposium series, vol. 90, p. 66, American Chemical Society, Washington DC.

Gibbs, J. W. 1906 *The Scientific Papers of J. William Gibbs, Vol. I: Thermodynamics.* Longmans Green & Co. (Dover Reprint 1961).

Gifford, W. A. & Scriven, L. E. 1971 On the attraction of floating particles. *Chem. Engng Sci.* **26**, 287–297.

Glowinski, R., Pan, T. W., Hesla, T. I. & Joseph, D. D. 1999 A distributed Lagrange multiplier/fictitious domain method for particulate flows. *Intl J. Multiphase Flow* **25**, 755.

Glowinski, R. & Pironneau, O. 1992 Finite element methods for Navier-Stokes equations. *Annu. Rev. Fluid Mech.* **24**, 167.

Glowinski, R., Tallec, P., Ravachol, M. & Tsikkinis, V. 1992 In *Finite Elements in Fluids*, Vol 8, chap 7 (ed. T. J. Chung). Hemisphere Publishing Corp., Washington DC.

Goldman, A. J., Cox, R. G. & Brenner, H. 1967 Slow viscous motion of a sphere parallel to a plane wall—I Motion through a quiescent fluid. *Chem. Engng Sci.* **22**, 637–653.

Grzybowski, B. A., Bowden, N., Arias, F., Yang, H. & Whitesides, G. M. 2001 Modeling of menisci and capillary forces from the millimeter to the micrometer size range. *J. Phys. Chem.* B 105, 404–412.

Hesla, T. I. & Joseph, D. D. 2004 The maximum contact angle at the rim of a heavy floating disk. *J. Colloid Interface Science*, **279**, 186.

Hirt, C. W. & Nichols, B. D. 1981 Volume of fluid (VOF) methods for the dynamics of free boundaries. *J. Comput. Phys.* **39**, 201.

Joseph, D. D. 2002 Interrogations of Direct Numerical Simulation of Solid-Liquid Flows, Web based book: http://www.efluids.com/efluids/books/efluids_books.htm.

Joseph, D. D., Wang, J., Bai, R., Yang, B. H. & Hu, H. H. 2003 Particle motion in a liquid film rimming the inside of a rotating cylinder. *J. Fluid Mech.* **496**, 139.

Kamal, M. R., Goyal, S. K. & Chu, E. 1988 Simulation of injection mold filling of viscoelastic polymer with fountain flow. *AIChE J.* **34**, 94.

Katoh, K., Fujita, H. & Imazu, E. 1992 Motion of a particle floating on a liquid meniscus surface. *J. Fluids Engng* **114**, 411.

Keller, J. B. 1998 Surface tension force on a partly submerged body. *Phys. Fluids* **10**, 3009.

Kistler, S. F. & Scriven, L. E. 1994 The teapot effect: sheet-forming flows with deflection, wetting and hysteresis. *J. Fluid Mech.* **263**, 19.

Kralchevsky, P. A., Paunov, V. N., Denkov, N. D., Ivanov, I. B. & Nagayama, K. 1993 Energetical and force approaches to the capillary interactions between particles attached to a liquid-fluid interface. *J. Colloid Interface Sci.* **155**, 420.

Kralchevsky, P. A. & Nagayama, K. 2000 Capillary interactions between particles bound to interfaces, liquid films and biomembranes. *Adv. Colloid Interface Sci.* **85**, 145.

Kralchevsky, P. A., Paunov, V. N., Denkov, N. D. & Nagayama, K. 1992 Capillary Meniscus Interactions between Colloidal Particles Attached to a Liquid – Fluid Interface. *J. Colloid Interface Sci.* **151** 79.

Kralchevsky, P. A., Paunov, V. N., Denkov, N. D. & Nagayama, K. 1994 Capillary Image Forces: II. Theory. *J. Colloid Interface Sci.* **167**, 47.

Majumdar, S. R., O'Neill, M. E. & Brenner, H. 1974 Note on the slow rotation of a concave spherical lens on bowl in two immiscible semi-infinite viscous fluids. *Mathematika.* **21**, 147–154.

Manon, V. B. & Wasan, D. T. 1986 Particle-fluid interactions with application to solid-stabilized emulsions. Part 1, The effect of asphaltene adsorption. *Colloids Surf.* **19**, 89.

Marchuk, G. I. 1990 Splitting and alternate direction methods. In *Handbook of Numerical Analysis* (ed. P. G. Ciarlet & J. L. Lions). Volume I, p. 197. North-Holland.

Nicolson, M. M. 1949 The interaction between floating particles. *Proc. Camb. Phil. Soc.* **45**, 288.

Osher, S. & Sethian, J. A. 1988 Fronts propagating with curvature-dependent speed: Algorithms based on Hamilton-Jacobi formulations. *J. Comput. Phys.* **83**, 12.

Petkov, J. T., Denkov, N. D., Danov, K. D., Velev, O. D., Aust, R. & Durst, F. 1995 Measurement of the drag coefficient of spherical particles attached to fluid interfaces. *J. Colloid Interface Sci.* **172**, 147.

Pillapakkam, S. B. & Singh, P. 2001 A Level Set Method for computing solutions to viscoelastic two-phase flow. *J. Computat. Phys.* **174**, 552.

Poynting, J. H. & Thompson, J. J. 1913 *A Text-book of Physics: Vol. 1, Properties of Matter*. pp. 153–155. C. Griffith & Co. Ltd, London.

Princen, H. M. 1969 Equilibrium shape of interfaces, drops and bubbles. Rigid and deformable particles at interfaces. In *Surface and Colloid Science* (ed. E. Matijevie), vol. 2, p. 1. Interscience.

Rapacchietta, A. V. & Neumann, A. W. 1977 Force and free-energy analyses of small particles at fluid interfaces: II. Spheres. *J. Colloid Interface Sci.* **59**, 555.

Redoev, B., Nedjalkov, M. & Djakovich, V. 1992 Brownian motion at liquid-gas interfaces. I. Diffusion coefficients of maroparticles at pure interfaces. *Langmuir* **8**, 2962.

Ryskin, G. & Leal, L. G. 1984 Numerical solution of free-boundary problems in fluid mechanics. Part 1: The finite-difference technique. *J. Fluid Mech.* **148**, 1.

Saif, T. A. 2002 On the capillary interaction between solid plates forming menisci on the surface of a liquid. *J. Fluid Mech.* **453**, 321.

Scardovelli, R. & Zaleski, S. 1999 Direct Simulation of Free-surface and interfacial flow. *Annu. Rev. Fluid Mech.* **31**, 567.

Schneider, Y. C., O'Neill, M. E. & Brenner, H. 1973 On the slow viscous rotation of a body straddling the interface between two immiscible semi-infinite fluids. *Mathematika* **20**, 175.

Singh, P. & Hesla, T. I. 2004 Torque on floating particles. *J. Colloid Interface Sci.* **280**, 542.

Singh, P., Hesla, T. I. & Joseph, D. D. 2003 A modified distributed Lagrange multiplier/fictitious domain method for particulate flows with collisions. *Intl J. Multiphase Flows* **29**, 495.

Singh, P., Joseph, D. D., Hesla, T. I., Glowinski, R. & Pan, T. W. 2000A distributed Lagrange multiplier/fictitious domain method for viscoelastic particulate flows. *J. Non-Newtonian Fluid Mech.* **91**, 165.

Singh, P. & Leal, L. G. 1993 Finite element simulation of the start-up problem for a viscoelastic problem in an eccentric cylinder geometry using third-order upwind scheme. *Theoret. Comput. Fluid Dyn.* **5**, 107.

Sussman, M. 2001 *An Adaptive Mesh Algorithm for Free Surface Flows in General Geometries, Adaptive Method of lines* (ed. A. Vande Wouwer, Ph. Saucez & W. E. Scheisser), p. 207. Chapman and Hall/CRC.

Sussman, M., Smereka, P. & Osher, S. 1994 A level set approach for computing solutions to incompressible two-phase flow. *J. Comput. Phys.* **114**, 146.

Unverdi, S. O. & Tryggvason, G. 1992 A front-tracking method for viscous, incompressible, multi-fluid flows. *J. Comput. Phys.* **100**, 25.

Wakiya, S. 1957 *Niigata Univ. College of Engng. Res. Rep.* 6. Nagoaka, Japan (March 30).

Wang, J., Bai, R. & Joseph, D. D. 2005 Experiments on floating particles, unpublished notes.

Yan, N. & Masliyah, J. H. 1994 Absorption and desorption of clay particles at the oil-water interface. *J. Colloid Interface Sci.* **168**, 386.